Title	Accurate effective-one-body waveforms of inspiralling and coalescing black-hole binaries
Authors	Damour, Thibault;Nagar, Alessandro;Hannam, Mark;Husa, Sascha;Bruegmann, Bernd
Publication date	2008
Original Citation	Damour, T., Nagar, A., Hannam, M., Husa, S. and Brügmann, B. (2008) 'Accurate effective-one-body waveforms of inspiralling and coalescing black-hole binaries', Physical Review D, 78(4), 044039 (24pp). doi: 10.1103/PhysRevD.78.044039
Type of publication	Article (peer-reviewed)
Link to publisher's version	https://journals.aps.org/prd/abstract/10.1103/PhysRevD.78.044039 - 10.1103/PhysRevD.78.044039
Rights	© 2008, American Physical Society
Download date	2024-05-02 03:54:47
Item downloaded from	https://hdl.handle.net/10468/4573

Accurate effective-one-body waveforms of inspiralling and coalescing black-hole binaries

Thibault Damour,[1,2] Alessandro Nagar,[1,2,3] Mark Hannam,[4,5] Sascha Husa,[4,6] and Bernd Brügmann[4]

[1]*Institut des Hautes Etudes Scientifiques, 91440 Bures-sur-Yvette, France*
[2]*ICRANet, 65122 Pescara, Italy*
[3]*INFN, sez. di Torino, Via P. Giuria 1, Torino, Italy*
[4]*Theoretical Physics Institute, University of Jena, 07743, Jena, Germany*
[5]*Physics Department, University College Cork, Cork, Ireland*
[6]*Max-Planck-Institut für Gravitationsphysik, Albert-Einstein-Institut, Potsdam-Golm, Germany*

The effective-one-body (EOB) formalism contains several flexibility parameters, notably a_5, v_{pole}, and $\bar{a}_{\text{RR}}$. We show here how to jointly constrain the values of these parameters by simultaneously best-fitting the EOB waveform to two, independent, numerical relativity (NR) simulations of inspiralling and/or coalescing binary black-hole systems: published Caltech-Cornell *inspiral* data (considered for gravitational wave frequencies $M\omega \leq 0.1$) on one side, and newly computed *coalescence* data on the other side. The resulting, approximately unique, "best-fit" EOB waveform is then shown to exhibit excellent agreement with NR coalescence data for several mass ratios. The dephasing between this best-fit EOB waveform and published Caltech-Cornell inspiral data is found to vary between -0.0014 and $+0.0008$ radians over a time span of $\sim 2464M$ up to gravitational wave frequency $M\omega = 0.1$, and between $+0.0013$ and -0.0185 over a time span of $96M$ after $M\omega = 0.1$ up to $M\omega = 0.1565$. The dephasings between EOB and the new coalescence data are found to be smaller than: (i) ± 0.025 radians over a time span of $730M$ (11 cycles) up to merger, in the equal-mass case, and (ii) ± 0.05 radians over a time span of about $950M$ (17 cycles) up to merger in the 2:1 mass-ratio case. These new results corroborate the aptitude of the EOB formalism to provide accurate representations of general relativistic waveforms, which are needed by currently operating gravitational wave detectors.

I. INTRODUCTION

The effective-one-body (EOB) formalism [1–4] is an analytical approach which aims at accurately describing both the motion of, and the radiation from, coalescing binary black holes. The EOB method uses, as basic input, high-order post-Newtonian (PN) expanded results (see [5] for a review of the PN-theory of gravitationally radiating systems). However, one of the key ideas in the EOB method is to avoid using PN results in their original "Taylor-expanded" form (symbolically $f^{\text{Taylor}}(v/c) = c_0 + c_1 v/c + c_2(v/c)^2 + \cdots + c_n(v/c)^n$), but, instead, to "repackage" them in some *resummed* form, i.e., symbolically, to replace $f^{\text{Taylor}}(v/c)$ by some nonpolynomial function $f^{\text{EOB}}(v/c)$, defined so as to incorporate some of the expected nonperturbative features of the (unknown) result. This repackaging is crucial for being able to bypass the strong limitations of PN results. Indeed, by itself PN theory is unable to go beyond the (adiabatic) *early inspiralling* stage of black hole coalescence,[1] while the EOB method is able to describe, in a continued manner, the full coalescence process: adiabatic early inspiral, nonadiabatic late inspiral, plunge, merger, and ring-down. The EOB method comprises three, rather separate, parts:

(1) a description of the conservative (Hamiltonian) piece of the dynamics of two black holes;

(2) an expression for the radiation-reaction force $\mathcal{F}_\varphi$ that supplements the Hamiltonian dynamics;

(3) a description of the gravitational wave (GW) signal emitted by a coalescing binary system.

For each one of these parts, the EOB method uses special resummation techniques, inspired by specific results going beyond perturbation theory. For instance, the resummation of the EOB Hamiltonian (part 1) was inspired by a specific resummation of ladder diagrams used to describe positronium energy states in quantum electrodynamics [6]. The resummation of the radiation-reaction force $\mathcal{F}_\varphi$ was inspired by the Padé resummation of the flux function introduced in Ref. [7]. As for part 3, i.e. the EOB description of the gravitational radiation emitted by a coalescing black-hole binary, it was mainly inspired by the classic work of Davis, Ruffini, and Tiomno [8], which discovered the transition between the plunge signal and a ringing tail when a particle falls into a Schwarzschild black hole.

Before the availability of reliable numerical simulations, the EOB method made several quantitative and qualitative predictions concerning the dynamics of the coalescence, and the corresponding GW radiation, notably: (i) a blurred transition from inspiral to a "plunge" that is just a smooth continuation of the inspiral, (ii) a sharp transition, around the merger of the black holes, between a continued inspiral and the ring-down signal, and (iii) estimates of the radiated energy, and of the spin of the final black hole (the latter

---

[1]See Appendix B for a new confirmation of this fact.

estimates were made both for nonspinning binaries [2] and for spinning ones [9]). Those predictions have been broadly confirmed by the results of recent numerical simulations performed by several independent groups (for a review of numerical relativity results see [10]). The recent breakthroughs in numerical relativity (NR) [11–15] open the possibility of acquiring some knowledge about binary black-hole coalescence that goes beyond what either PN theory, or its resummed avatars (such as the EOB), can tell us. Actually, it was emphasized early on [4,16,17] that the EOB method should be considered as a *flexible* structure, containing several parameters representing (yet) uncalculated results, that would need NR results (or real observational data) to be determined. For instance, Refs. [4,16] introduced a parameter (here denoted as a_5) representing uncalculated 4 PN, and higher, contributions to the crucial EOB "radial potential" $A(R)$. Reference [17] introduced several more EOB *flexibility parameters*, notably v_{pole} (entering the Padé resummation of the radiation-reaction force) and a parameter (here replaced by $\bar{a}_{\text{RR}}$) describing uncalculated nonquasicircular (NQC) contributions to the radiation reaction. Recently, Ref. [18] augmented the list of EOB flexibility parameters by introducing two parameters (here denoted as a and b) representing NQC contributions to the waveform, as well as two parameters, t_m and δ (together with the choice of an integer p), describing the "comb" used in matching the inspiralling and plunging waveform to the ring-down one. Each one of these EOB flexibility parameters (a_5, v_{pole}, $\bar{a}_{\text{RR}}$, a, b, t_m, δ, p) parametrizes a *deformation*[2] of the originally defined EOB. Each direction of deformation, e.g., $\partial/\partial a_5$, hopefully adds some "missing physics" that either has not yet been calculated because of technical difficulties,[3] or represent only an *effective* description of a complicated, nonperturbative process which is not directly formalizable in a calculable way. In both cases, the EOB programme aims at using NR results to determine the "best-fit" values of the flexibility parameters; i.e., the values that, hopefully, allow an analytical EOB waveform to *accurately* represent the exact general relativistic inspiralling and coalescing waveform. Note that, in this paper, we will not use the terminology of *faithful* (versus *effectual*) waveforms [7]. Indeed, this ter-

minology refers to particular measures of the closeness of two waveforms (called "faithfulness", $\mathcal{F}$, and "effectualness", $\mathcal{E}$ in [17]) which are based on specific ways of maximizing normalized overlaps. These measures are not the best suited for our present purpose because they are detector dependent (through the use of the detector's spectral noise curve $S_h(f)$ in the Wiener scalar product $\langle X, Y \rangle$, see e.g., Eqs. (6.1) and (6.2) of [17]). By contrast, we are interested here in hopefully showing that EOB waveforms can be "close" to general relativistic ones in a much stronger mathematical sense, say in the time-domain L_∞ norm: $\sup_{t\in[t_1,t_2]}|h^{\text{EOB}}(t) - h^{\text{exact}}(t)| < \varepsilon$. Actually, the most important "closeness," for data analysis purposes, is the closeness of the phases. Therefore we shall primarily consider the time-domain *phase* L_∞ norm: $\|\Delta\phi\|_\infty \equiv \inf_{\tau,\alpha}\sup_{t\in[t_1,t_2]}|\phi_{22}^{\text{EOB}}(t + \tau) + \alpha - \phi_{22}^{\text{NR}}(t)|$, where we minimize over the two arbitrary parameters τ (time-shift) and α (phase-shift). When $\|\Delta\phi\|_\infty$ is smaller than ε for most physically relevant intervals $[t_1, t_2]$, we shall say that the (time-domain) EOB waveform $h^{\text{EOB}}(t)$ is an *ε-accurate* representation of $h^{\text{exact}}(t)$.

The program of determining the "best-fit" flexibility parameters by comparing EOB predictions to NR results has been initiated in several works [16,18,20–22] (see also [23–25] for other works involving the comparison of EOB waveforms to NR ones). For some parameters,[4] it has already been possible to determine them, or, at least, to find a rationale that allows one to fix them in a near-optimal manner. For instance, it was found in Ref. [18] that $p = 2$, i.e. the use of $2p + 1 = 5$ matching points and 5 corresponding positive-frequency QNMs was optimal from a practical point of view, in the sense that smaller values led to visibly worse fits, while higher values led to only a rather marginal improvement. We shall therefore fix p to the value $p = 2$. Concerning the "central matching time" t_m, previous work [18,20,22] has found that it was near optimal to choose (as advocated in [2]) t_m to be the so-called "EOB light-ring crossing" time, i.e. the EOB dynamical time when the EOB orbital frequency Ω reaches its maximum. Concerning the matching-comb width parameter $\delta = \Delta t/(2p)$ (where Δt is the total width of the matching interval), Refs. [18,22] found that $\delta = 1.7M_{\text{final}}$ (corresponding to $\Delta t = 4\delta = 6.8M_{\text{final}}$) yielded a good result. Here M_{final} denotes the mass of the final black

---

[2]We use here the word *deformation* in the mathematical sense. Ideally we would like the list of EOB flexibility parameters to describe a kind of *versal deformation* of the original EOB, i.e. a multiparameter family which is general enough to encompass all the physics contained in real GW coalescence signals, starting from the originally defined EOB waveform, which was based on a rather coarse representation of the coalescence waveform.

[3]For instance, the exact, general relativistic value of a_5 [or, rather, of the ν-dependent coefficient $a_5(\nu) = \nu a_5 + \nu^2 a_5' + \cdots$ of $(GM/c^2R)^5$ in $A(R)$] has not yet been calculated simply because it would represent a huge technical challenge, involving a 4 PN (and 4-loop) generalization of the rather involved 3 PN (and 3-loop) work that led to the unique determination of the lower-order coefficient $a_4(\nu)$ [5,19].

[4]Note that several of the EOB flexibility parameters listed above refer to the recently introduced resummed 3^{+2}-PN accurate EOB waveform [18,21] and to the comb matching procedure of Ref. [18]. The EOB dynamics and waveform used in the works of Buonanno and collaborators differ in several ways from the dynamics and waveform used by us, notably: (i) a radiation-reaction force of lesser PN accuracy, and without NQC corrections, (ii) a waveform of "Newtonian" accuracy without NQC corrections, and (iii) a simpler matching procedure between the plunge and the ring-down involving only three (positive-frequency) quasinormal modes (QNM) and an instantaneous matching (as used in some of the original EOB papers [2,26]).

hole. Here also, we fix $t_m = t_{\rm EOB}^{\rm light\text{-}ring}$, and $\delta = 1.7 M_{\rm final}$. Moreover, we shall discuss below a rationale allowing one to fix the parameters a and b.

Summarizing: the only EOB flexibility parameters which have not yet been uniquely determined are a_5, $v_{\rm pole}$, and $\bar{a}_{\rm RR}$. Some recent works [20–22] have explored the influence of these parameters on the EOB waveform and have made initial steps towards determining "best-fit" values for these parameters; i.e., values leading to an optimal agreement with NR data. In particular, Ref. [20] found that the *faithfulness* $\mathcal{F}$ (in the sense of Sec. VIA of Ref. [17]) of restricted EOB waveforms against NASA-Goddard NR coalescence waveforms was largest when[5] a_5 belongs to some rather wide interval, say [20, 100], centered around $a_5 \sim 60$. On the other hand, Ref. [21] found that the *accuracy* (in the sense of the L_∞ norm of the phase difference) of the resummed 3^{+2}-PN EOB waveform[6] with respect to the high-accuracy Caltech-Cornell (CC) NR long-inspiral waveform was at its best when a_5 belonged to an interval $\sim$[10, 80] centered around $a_5 \sim 40$. The influence of the flexibility parameter $v_{\rm pole}$ was studied in Refs. [21,22]. It was found that, for any given values of a_5 and $\bar{a}_{\rm RR}$, *and for any given NR waveform*, there existed a well-determined value of $v_{\rm pole}$ that minimized the phase difference between EOB and NR (see below for a more precise formulation). However, those previous EOB-NR comparisons limited themselves to considering one NR data set at a time (the published Caltech-Cornell inspiral data for Ref. [21], and some Albert Einstein Institute (AEI) coalescence data for Ref. [22]).

The aim of the present paper is to go beyond this piece-meal consideration of NR data and to best fit (*in phase*) the flexed EOB waveform, $h^{\rm EOB}(a_5, v_{\rm pole}, \bar{a}_{\rm RR}; t)$, *simultaneously* to several independent NR waveform data (namely inspiral and coalescence data produced by the Jena group and reported here, and published inspiral Caltech-Cornell data). Our main result will be that the best-fit values of the three remaining EOB flexibility parameters $(a_5, v_{\rm pole}, \bar{a}_{\rm RR})$ are approximately determined, in the sense that they must all take values in relatively small, correlated, intervals. It is then found that the resulting, approximately unique, best fitted EOB waveform exhibits a remarkable agreement (modulo differences compatible with estimated numerical errors), both in phase and in modulus, not only with the data that we use in the fit (i.e., *equal-mass* Jena data and *equal-mass* Caltech-Cornell data considered for $M\omega \leq 0.1$), but also with other NR data (namely, *unequal-mass* Jena data and Caltech-Cornell data *after $M\omega = 0.1$*).

Our work focusses on the comparison between the EOB predictions and NR data because the EOB method is the only existing analytical approach which: (i) incorporates, in an exact manner, all the theoretical knowledge acquired through many years of post-Newtonian studies, (ii) provides waveforms covering the full coalescence process from early inspiral to ring-down, and (iii) can describe spinning binaries (see, in this respect Refs. [4,27]). However, as some studies have emphasized the nice properties of one specific PN approximant, called TaylorT4 in [28] (for consistency with the T1, T2, and T3 Taylor approximants considered in [29]), we shall discuss it briefly in Appendix B, though it does not satisfy our requirements (ii) above, namely, that of providing waveforms covering the full coalescence process.

This paper is organized as follows. In Sec. II we briefly describe the numerical simulations, whose results we use in the following. Section III summarizes the definition of the 3^{+2}-PN accurate EOB waveform that we use. Section IV is the central section of this work: it shows how the simultaneous comparison of EOB to two different NR data sets allows one to determine a small range of "best-fit" (correlated) EOB flexibility parameters a_5, $v_{\rm pole}$ and $\bar{a}_{\rm RR}$. Section V selects central values for the best-fit parameters and discusses in detail the agreement between the EOB waveform and the Jena NR waveform, for various mass ratios. The paper ends with a concluding section, followed by two Appendices. Appendix A is devoted to the issue of determining the metric waveform $h(t)$ from the curvature waveform $\psi_4(t)$, while Appendix B discusses the TaylorT4 approximant. Except when otherwise specified, we use in this paper units such that $G = c = 1$.

II. NUMERICAL RELATIVITY SIMULATIONS

Numerical simulations were performed with the BAM code [30,31], which evolves black-hole binaries using the "moving-puncture" approach [12,13]. The relevant physical and numerical parameters for our simulations are presented in Table I; note that the results from the equal-mass simulations were presented in [32], which also contains extensive error analysis and comparison with standard post-Newtonian inspiral approximants. These results are also in good agreement with those of [28] over the shared frequency range. We shall present below an explicit comparison of the phase of the waveform of Ref. [28] with the one of our equal-mass simulation.

A. Initial data

Following the moving-puncture approach we set up initial data containing two black holes via a Brill-Lindquist-like wormhole construction [33], where the additional asymptotically flat end of each wormhole is compactified to a point, or "puncture." The entire 2-wormhole topology can thus conveniently be represented on R^3. It has long been understood how to set up such puncture initial

---

[5]Note that Ref. [20] uses the notation λ for a_5.

[6]We refer to the PN accuracy of this waveform as 3^{+2}PN because it includes not only the known comparable mass 3 PN waveform corrections, but also the test-mass limit of the 4 PN and 5 PN waveform amplitude corrections [21].

TABLE I. Details of the simulations discussed in the test. From left to right, the columns report: mass ratio $q = m_2/m_1$; symmetric mass ratio $\nu = m_1 m_2/(m_1 + m_2)^2$; initial coordinate separation D of the punctures; initial ADM mass; initial tangential (p_t) and radial (p_r) momentum of the black holes; mass and dimensionless spin parameter $j_f = J_f/M_f^2$ of the final black hole; mass and dimensionless spin parameter j_f^{ring} and M_f^{ring}/M of the final black hole obtained only from the ring-down; dominant (quasinormal-mode) frequency of the ring-down. Quantities are scaled by the total initial black hole mass $M = m_1 + m_2$ as indicated.

q	ν	D/M	M_{ADM}/M	$\lvert p_t/M\rvert$	$10^3 \times \lvert p_r/M\rvert$	M_f/M	j_f	M_f^{ring}	j_f^{ring}	$M\sigma_{2220}^+$
1	1/4	12	0.991 225	0.085 035	0.053 729	0.9514 ± 0.0016	0.687 ± 0.002	0.962	0.690	$0.0850 + i0.5521$
2	2/9	10	0.990 901	0.085 599	0.794 821	0.96 ± 0.003	0.625 ± 0.004	0.977	0.635	$0.0856 + i0.5214$
4	4/25	10	0.993 522	0.061 914	0.043 332	0.978 ± 0.003	0.472 ± 0.004	0.990	0.487	$0.0874 + i0.4683$

data, and, in particular, how to avoid working with divergent quantities [34–37]. More recently it has turned out that the gauge conditions used in the moving-puncture approach actually allow a simpler representation of the black-hole interior during the evolution: the black-hole throat is pushed an infinite proper distance away from the horizon, and the initial puncture geometry is replaced by a new compactified asymptotics with a milder singularity [38–40].

One key element of the simplicity of the moving-puncture approach is that black holes can be modeled on a Cartesian numerical grid without the need to deal with black-hole excision techniques. Another is that the assumption of an initially conformally flat spatial geometry yields a very simple way to generate any number of moving, spinning black holes [36,41]. Note. however, that the puncture initial data are not restricted to conformal flatness *a priori* [34,35,37], and generalizations that better model spinning black holes have been suggested [42,43].

Assuming conformal flatness for the initial data, and assuming the extrinsic curvature of the initial slice to be within the class of nonspinning Bowen-York solutions, the freedom in specifying initial data comprises the masses, locations and momenta of each black hole.

The mass of each black hole, M_i ($i = 1, 2$), is specified in terms of the Arnowitt-Deser-Misner (ADM) mass at each puncture, which is, to a very good approximation [44–46] equal to the irreducible mass [47,48] of the apparent horizon

$$M_i = \sqrt{\frac{A_i}{16\pi}},\qquad(1)$$

where A_i is the area of the apparent horizon. We identify this mass with the mass (denoted below m_i) used in post-Newtonian theory. This assumption will only hold exactly in the limit where the black holes are infinitely far apart and stationary, but we consider any error in this assumption as part of the error due to starting the simulation at a finite separation.

The constraint equations for black-hole binary puncture initial data are solved using a pseudospectral code [49], and resampled for our finite-difference grid using high-order polynomial interpolation [31].

We want to specify initial data for nonspinning black holes in the center-of-mass frame, such that the trajectories correspond to quasicircular inspiral, i.e. the motion is circular at infinite separation, and the eccentricity vanishes. Following [50], we obtain the initial momenta of the black holes from a post-Newtonian inspiral calculation, using a 3PN-accurate conservative Hamiltonian [19], and 3.5PN accurate beyond leading order orbit-averaged radiation flux [51,52]. We have measured the eccentricity from oscillations in the separation and frequency as described in [50], and have obtained the values 0.002, 0.003, 0.005, for mass ratios $q = 1$, 2, and 4, respectively.

B. Numerical evolution

We use the BSSN formulation of the Einstein equations [53,54] for time evolution, which are formulated in terms of a conformal 3-metric $\tilde{\gamma}_{ij}$, related to the physical metric as

$$\tilde{\gamma}_{ij} = \chi\gamma_{ij}.\qquad(2)$$

Representing the conformal factor by the quantity χ has the advantage that, when dealing with puncture data, the conformal factor χ conveniently vanishes at each puncture [12]. Details of our implementation of the BSSN/moving-puncture system are described in [30]. We also need to choose a lapse and shift during the evolution to determine our coordinate gauge. As is common in the moving-puncture approach, we use the "1 + log" slicing condition [55]

$$\partial_0 \alpha = -2\alpha K,\qquad(3)$$

and the $\tilde{\Gamma}$-driver condition [56,57],

$$\partial_0 \beta^i = \tfrac{3}{4} B^i,\qquad(4)$$

$$\partial_0 B^i = \partial_0 \tilde{\Gamma}^i - \eta B^i,\qquad(5)$$

where $\partial_0 = \partial_t - \beta^i \partial_i$. The parameter η in the shift-condition effectively regulates the coordinate size of the apparent horizons, and is set to $\eta = 2/M$ in our simulations.

The Einstein evolution equations are solved numerically with standard finite-difference techniques as described in [30,31]. Spatial derivatives are approximated with sixth-

order accurate stencils. First order derivatives corresponding to Lie derivatives with respect to the shift vector are approximated with off-centered operators as described in [31], all other derivatives are approximated with centered finite-difference operators. Kreiss-Oliger artificial dissipation operators which converge to zero at fifth order are applied as described in [30,31]. Time evolution is performed with a fourth-order Runge-Kutta integration. Our box-based mesh refinement is described in [30]. Time interpolation errors in the mesh-refinement algorithm converge only at second order, but do not seem to contribute significantly to the error budget, as does the Runge-Kutta time integration.

The grid configurations we have used for our equal-mass runs are described in [32]. For the unequal-mass runs, we have used the 56, 64, 72-gridpoints configurations of [32], adding two further refinement levels to push the outer boundary further out by roughly a factor of 4. In order to be able to reuse our equal-mass grid configurations, we always choose the mass of the smaller black hole, which determines our resolution requirements, at $M_1 = 0.5$.

C. Wave extraction

The gravitational wave signal is extracted at different surfaces of constant radial coordinate by means of the Newman-Penrose Weyl tensor component ψ_4 [58,59] which is a measure of the outgoing transverse gravitational radiation in an asymptotically flat spacetime. At finite distance to the source the result depends on the coordinate gauge and the choice of a null tetrad. Our choice of tetrad and details of the wave extraction algorithm are described in detail in [30]. We choose our extraction surfaces at 40, 50, 60, 80, and 90M. In [32] we extrapolated the waveform amplitude (though not its phase) to the value that would be observed at infinity; in this work we deal with the raw numerical data at the farmost extraction radius, but use some extraction-radius-extrapolated results to provide uncertainty estimates. See next subsection.

The analysis carried out in this paper will use, as approximate asymptotic waveform, the curvature perturbation extracted at radius 90M, without any extrapolation (neither with respect to extraction radius, nor with respect to resolution). The comparisons between numerical data and analytical predictions done below will make use of *metric* (by contrast to curvature) waveforms. We discuss in Appendix A the integration procedure we used to compute the numerical metric waveform from the raw curvature waveform output of the simulations. In this paper, we focus on the $\ell = m = 2$ "quadrupolar" waveform.

D. Accuracy

1. The equal-mass case

A detailed error analysis was performed for the equal-mass waveforms in [32]. In this section, we will first summarize the results of that error analysis, and then complete it by more carefully quantifying the uncertainty in the phase. As we shall see, our refined estimate of the uncertainty in the phase will end up being *significantly lower* than the upper bound, 0.25 radians, quoted in [32].

The amplitude and phase of the equal-mass nonspinning waveforms show sixth-order convergence with respect to numerical grid resolution prior to merger, with a small drop in convergence order around merger time. Higher-accuracy results were constructed by Richardson extrapolation with respect to numerical resolution, and this procedure also allowed an estimation of the contribution to the uncertainty in the amplitude and phase from discretization error. The discretization error in the amplitude was found to be below 0.5%, while the discretization error in the phase was estimated to be below 0.01 radians. These are conservative error estimates obtained by observing the numerical errors over the course of the entire simulation. See, in particular, Fig. 4 in [32]. If we look at that figure we may conclude that the error estimate of the phase is extremely conservative, but one should also be aware that the quoted numerical phase error takes into account only instantaneous differences in the value of the waveform phase, but not secular drifts. When the analysis for [32] was performed, the authors hoped that the conservative value quoted would account for any phase drifts. We shall see below that, however, there might remain sources of secular drifts that are not yet well understood.

In addition to the discretization error, there is also an error due to measuring the waveform at a finite distance from the source. For both the waveform amplitude and phase, it was found in [32] that finite extraction radii errors were much larger than discretization errors. Prior to merger, the error in the amplitude was found to fall off as $1/R_{ex}^2$, where R_{ex} was the radiation extraction radius, and this observation allowed a clean extrapolation to $R_{ex} \rightarrow \infty$, and, once again, an estimate of the uncertainty in the amplitude. The uncertainty in the *extrapolated* amplitude was at most 2% before merger. Around merger time, the amplitude error falloff is dominated by a $1/R_{ex}$ term, and the uncertainty in the extrapolated amplitude grows to around 5%. However, in this paper we use the raw data calculated at the extraction radius $R_{ex} = 90M$, and as such the uncertainties are larger, as much as 5% over the entire simulation. The largest uncertainties in the finite-extraction-radius amplitude are at early times, when the amplitude is small, and around merger, when the dynamics are strongest.

In [32] the total phase uncertainty accumulated on a time interval of duration 1400M extending up to gravitational wave frequency $M\omega = 0.1$ was quoted as being 0.25 radians. This large value was an upper bound which was quoted in view of the difficulty in finding a robust method to extrapolate the phase to infinite extraction radius. These difficulties were related to the specific phase alignment

method which was used in [32]. There, one was first choosing some frequency at which to line up the phases and frequencies of waves from different extraction radii, and then attempting to perform an extrapolation. Although it is entirely valid to time- and phase-shift any number of waveforms to perform a comparison between them, it turned out that this is not an efficient way to perform a consistent extraction-radius extrapolation.

By contrast, for the purpose of the present paper we have performed a new study of the extraction-radius extrapolation which follows the strategy proposed in [28]. More precisely we used two similar, but different, phase alignment methods. The first one consists of simply introducing the "Newtonian retarded time," at the coordinate extraction radii R_{ex}, $u_N = t - R_{ex}$ and study the waves as function of u_N. Then, when attempting extrapolation with respect to R_{ex}, we find a clear $c_0(u_N) + c_2(u_N)/R_{ex}^2$ falloff in the error, and are able to make a clean extrapolation to infinity. We have also repeated the analysis with an extra $+c_3(u_N)/R_{ex}^3$ term in the fit.

The second method consists of using, inspired by the result in [28], the *a priori* more accurate definition of retarded time, $u_B = t - r_*$, where the (approximate) Regge-Wheeler tortoise coordinate r_* is (following [28]) defined as $r_* = R_{ex} + M_{ADM} + 2M_{ADM} \log[(R_{ex} + M_{ADM})/(2M_{ADM}) - 1]$. This improved choice of retarded time allows us again to perform a clean extrapolation to infinity. As when using u_N, we use two different fits: $c_0(u_B) + c_2(u_B)/R_{ex}^2$ and $c_0(u_B) + c_2(u_B)/R_{ex}^2 + c_3(u_B)/R_{ex}^3$. We then estimate the uncertainty in the phase of the farmost unextrapolated data, extracted at $R_{ex} = 90M$, by comparing the following five phases: (i) the raw phase ϕ_{90M} measured at $R_{ex} = 90M$, (ii) the phase ϕ_{N2}^∞ extrapolated using u_N and assuming a $1/R_{ex}^2$ falloff, (iii) the phase ϕ_{N3}^∞ extrapolated using u_N and assuming a $1/R_{ex}^2 + 1/R_{ex}^3$ falloff, (iv) the phase ϕ_{B2}^∞ extrapolated using u_B and assuming a $1/R_{ex}^2$ falloff, and (v) the phase ϕ_{B3}^∞ extrapolated using u_B and assuming a $1/R_{ex}^2 + 1/R_{ex}^3$ falloff. The differences between the phases are computed after they have been aligned by using the two-times pinching technique of Ref. [22] (which is reviewed in Sec. IV below). For consistency with our EOB-NR matching discussed in Sec. V below we use as "pinching" gravitational wave frequencies $\omega_1 \approx 0.1$ and $\omega_2 = 0.4717$. Note that these frequencies bracket the merger time. The four phase differences $\phi_{90M} - \phi_i^\infty$ where $i \in \{N2, N3, B2, B3\}$ are exhibited as functions of the numerical relativity coordinate time at $90M$, in Fig. 1. The triangles in the figure indicate the two times corresponding to the two pinching frequencies (ω_1, ω_2), while the vertical dashed lines indicate the time interval $[1200, 1900] \approx [t_L, t_R]$ which will turn out to be crucial for our analysis in Sec. V below. Several conclusions can be drawn from Fig. 1: First, the choice of retarded time, u_N or u_B, does not matter much for the extrapolation procedure. Second, though the phase
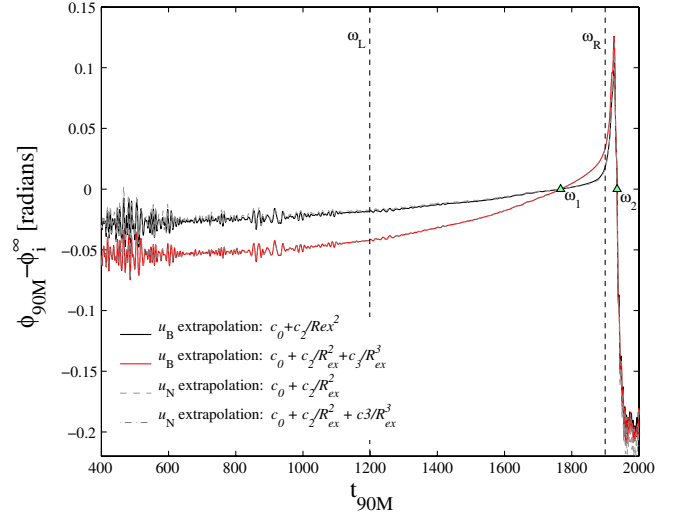

FIG. 1 (color online). Differences between the phase extracted at $R_{ex} = 90M$, and the phase extrapolated to infinity based on two choices of the retarded time and on two choices of the extrapolating polynomial, as described in the text. The choice of retarded time makes little difference to the result.

differences over the entire span of the simulation can reach values $\sim +0.13$ radians around merger time (peak at $t \approx 1930M$) and/or ~ -0.2 radians (during ring-down), they stay quite small during the time interval $[t_L, t_R]$ that we shall focus on in our analysis below.[7] Most importantly for the following the maximum phase differences over the interval $[t_L, t_R]$ stay within the rather small interval $(-0.042, +0.032)$ radians.

After this "internal" way of trying to estimate the numerical errors in the phase of our equal-mass simulation, let us consider an "external" way which consists in directly comparing the unextrapolated, 90M raw phase $\phi_{90M}(t)$ to the phase computed by Boyle *et al.* [28] and kindly communicated to us. In Fig. 2 we are directly comparing two phases: our unextrapolated $\phi_{90M}(t)$ and the resolution- and radius-extrapolated Caltech-Cornell curvature phase $\phi_{CC}(t)$. The phase difference $\Delta\phi_{22}^{CCJena} = \phi_{CC} - \phi_{90M}$ was plotted versus the Caltech-Cornell (curvature) frequency ω_{CC}. This phase difference was computed in the following way. First, we used the two-pinching frequencies $\omega_1 = 0.059517$ and $\omega_2 = 0.14976$ (indicated

---

[7]Note also that with the above choice of pinching times (ω_1, ω_2) the phase differences stay quite small, namely -0.06 radians, during the entire inspiral. However, this result sensitively depends on the way the phases have been matched. For instance, when using pinching frequencies $\omega_1 = \omega_2 = 0.1$ one observes maximum phase differences of $\sim +0.07$ radians at merger and ~ -0.45 radians during ring-down, while they stay between $(-0.03, 0)$ radians during the inspiral. On the other hand, when using pinching frequencies around merger, i.e., $\omega_1 = 0.36$ and $\omega_2 = 0.38$, one gets quite small phase differences during merger and ring-down, but one observes large dephasings at early times, that build up to -0.6 radians.
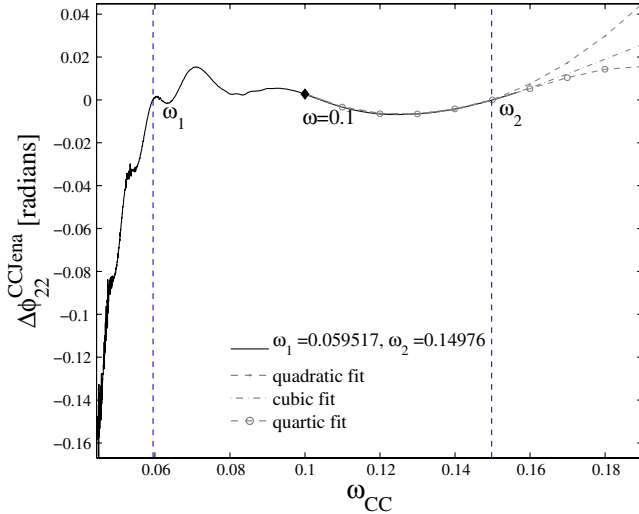
FIG. 2 (color online). Comparison between Caltech-Cornell and Jena actual numerical data: the phase difference $\Delta\phi_{22}^{\text{CCJena}} = \phi^{\text{CC}} - \phi_{90M}^{\text{Jena}}$ is shown versus Caltech-Cornell GW frequency ω_{CC}.

by two dashed vertical lines in the figure) to determine the time and phase shifts (τ, α), see below, then the result $\Delta\phi_{22}^{\text{CCJena}}(t_{\text{CC}}) = \phi_{\text{CC}}(t_{\text{CC}}) - (\phi_{90M}(t_{\text{CC}} + \tau) + \alpha)$ is plotted versus ω_{CC} instead of t_{CC}. In addition, since the Caltech-Cornell simulation extends only up to $\omega_{\text{CC}}^{\max} \sim \omega_2 \approx 0.15$, we have estimated three different possible extrapolations of the phase difference $\Delta\phi_{22}^{\text{CCJena}}$ beyond ω_2 and up to $\omega_{\text{R}} = 0.1898$.[8] These three different extrapolations were obtained by fitting $\Delta\phi(\omega_{\text{CC}})$ over the interval [0.1, 0.15] by three different polynomial functions of ω_{CC}: quadratic, cubic, and quartic. As we see in Fig. 2, the quadratic fit is the one which gives the worst possible phase difference over the interval $[\omega_{\text{L}}, \omega_{\text{R}}]$. We use this worst case as an estimate of the maximum phase difference between Caltech-Cornell and Jena phasings over $[t_{\text{L}}, t_{\text{R}}]$. More precisely, while the minimum value of $\Delta\phi_{22}^{\text{CCJena}}$ over the interval is -0.0068 radians, its maximum is $+0.044\,84$ radians (at ω_{R}, i.e., at the extreme right of Fig. 2). This corresponds to a two-sided CC-Jena phase difference (in the sense of footnote 12 of Ref. [22]) $\pm 1/2[0.044\,84 - (-0.0068)] = \pm 0.026$ radians over the interval $[\omega_{\text{L}}, \omega_{\text{R}}]$. As this difference *a priori* comprises many possible "noise sources" coming from comparing two very different simulations, with different wave extraction procedures, we consider that this is our best present estimate of the unknown "real" error on the difference $\phi_{90M} - \phi_{\text{CC}}$. In addition, as a recently published *upper limit* on the *total accumulated phase error* in the Caltech-Cornell data of Ref. [28] is 0.01 radians [60] (which is rather small), we

shall consider in the following that ± 0.026 radians provide our best current estimate of the real error on the equal mass ϕ_{90M} over the interval $[\omega_{\text{L}}, \omega_{\text{R}}]$. Note, in passing, that the internal error analysis procedure discussed above was giving a roughly comparable error estimate, namely, a two-sided phase difference $\pm 1/2(0.032 - (-0.042)) \sim \pm 0.037$ radians. However, we cannot rely on this internal analysis because it fails to explain the origin of a striking feature of Fig. 2, which is that, before the plateau of very small phase differences reached between frequencies 0.06 and 0.15, there is a steeper phase gradient which reaches -0.16 radians at $\omega = 0.044\,45$, roughly corresponding to the beginning of the Jena simulation. Part of this error may be due to residual eccentricity—a quick comparison with post-Newtonian results using the techniques described in [50] suggests that the phase error from a residual eccentricity of $e \sim 0.002$ could be as much as 0.05 radians. We feel, however, that most of the error comes from some secular drift at early times which is not yet well understood.

2. The unequal-mass cases

For the unequal-mass case 2:1, we find similar results, namely, that the finite extraction radii dominate the error, and the amplitude error is below 5% prior to merger. As for the accumulated phase error in the $700M$ time span up to $M\omega = 0.1$, we did not carry out the radius extrapolation analysis discussed above in the unequal-mass case. As a rough upper limit we quote an accumulated phase error of 0.15 radians. In contrast to the equal-mass case, the falloff in the amplitude error with respect to radiation extraction radius is not so clean around merger time, preventing us from performing an accurate extrapolation to infinity. As such, we would conservatively give an uncertainty estimate of 10% of the amplitude at merger and later.

In the unequal-mass case 4:1, the case is different again: here the discretization error dominates the phase error, suggesting that higher-resolution simulations are needed. Our estimate for the accumulated phase uncertainty up to $M\omega = 0.1$ is 0.25 radians, based entirely on discretization error. For the amplitude we estimate that the uncertainty is similar to that in the 1:2 case, i.e., around 5% prior to merger, and 10% after that time.

E. Final parameters of the black hole

The final mass of the black hole is obtained by subtracting the radiated energy from the initial mass. While the initial mass (the ADM mass) is known very accurately from the solution of the constraints with spectral methods [49], the radiated energy is less accurate and dominates the errors of the final mass and Kerr spin parameter. The radiated energy is not very accurate, due to the loss of accuracy in the wave signal at merger time for the equal-mass case (leading to a conservative error estimate of 4%), and the problems of extrapolation in radius and gridspacing

---

[8]Note that $\omega_1 = \omega_{\text{L}}$ corresponds to the lower limit t_{L} of the crucial EOB-NR comparison interval used in Sec. IV, while ω_{R} corresponds to its upper limit t_{R}.

for the unequal-mass cases, which lead us to a conservative error estimate of 10% in those cases.

The error in the radiated energy also dominates computing the quantity $j_f = J/M^2$, where we either compute J from a surface integral as in [30] and M as described above, or we calculate j_f itself from the ring-down. The error in computing the angular momentum J from a surface integral falls off very quickly with separation. The dominant error in this quantity comes from high-frequency numerical noise in the integrals, which is however much smaller than the error in j_f resulting from errors in the final mass.

To determine the mass and spin parameter of the final black hole from the ring-down, we have performed two types of fits to the dominant mode. First, the quality factor has been obtained from a fit to the dominant quasinormal mode[9] of the *complex* ring-down waveform. This fit was performed by a nonlinear least-squares Gauss-Newton method, using $\exp(-\sigma t + \rho)$ as a parameter-dependent template [with two *complex* parameters (σ, ρ)], and an appropriate time interval during the ring-down (chosen by minimizing the post-fit residual). Then, from the best-fit value of σ (i.e., the QNM dominant complex frequency σ_{2220}^+), we computed the values of $(M_f^{\rm ring}, j_f^{\rm ring})$ of the final black hole by using the interpolating fits given in Appendix E of [61]. The triplets $(M_f^{\rm ring}/M, j_f^{\rm ring}, M\sigma_{2220}^+)$ are listed in Table I.

This method does not require knowledge of the final mass, but is actually not well conditioned due to the shape of the curve $j(\omega)$. Better accuracy is obtained by only using the real part of the frequency, then again, the error in j is dominated by the error in the radiated energy. The values are consistent with the values obtained from the surface integrals for the angular momentum J. The numbers M_f and j_f quoted in Table I are consistent with both methods, and with the analytical fit for j_f published for shorter and less accurate waveforms in [62]. By contrast $(M_f^{\rm ring}, j_f^{\rm ring})$, are "best-fit" values that will be used below to compute the EOB ring-down waveform.

III. THE EOB WAVEFORM

We shall not review here the EOB formalism, which has been described in several recent publications [20–22,24,63]. We refer to these papers, and notably to Refs. [21,24], for detailed definitions of the dynamics and of the waveform. Let us only indicate here a few of the crucial elements of the EOB implementation that we use here. We recall below the main ingredients of the EOB formalism, focusing on the appearance of the various EOB flexibility parameters.

(i) The EOB Hamiltonian $H_{\rm real}$ describes the conservative part of the relative two-body dynamics. We use

for the crucial "radial potential" $A(r)$ entering this Hamiltonian the P_4^1 Padé resummation of

$$A^{\rm Taylor}(a_5, \nu; u) = 1 - 2u + 2\nu u^3 + a_4 \nu u^4 + a_5 \nu u^5, \qquad (6)$$

where [3,19]

$$a_4 = \frac{94}{3} - \frac{41}{32}\pi^2, \qquad (7)$$

where a_5 is the 4 PN flexing parameter introduced in [4], and where[10] $u = 1/r$.

(ii) The EOB *radiation-reaction force* $\mathcal{F}_\varphi(v_{\rm pole}, \bar{a}_{\rm RR}, \nu)$, that we shall use here, has the form

$$\mathcal{F}_\varphi(v_{\rm pole}, \bar{a}_{\rm RR}, \nu) = f_{\rm RR}^{\rm NQC}(\bar{a}_{\rm RR})\mathcal{F}_\varphi^0(v_{\rm pole}, \nu), \quad (8)$$

where $\mathcal{F}_\varphi^0(v_{\rm pole}, \nu)$ is defined as a Padé resummation [7] of its Taylor expansion. See Eq. (17) of [18] where $f_{\rm DIS}$ is the P_4^4 Padé resummation of $(1 - v/v_{\rm pole})\hat{F}^{\rm Taylor}(v; \nu)$. In addition, the factor $f_{\rm RR}^{\rm NQC}$ is a nonquasicircular (NQC) correction factor of the form

$$f_{\rm RR}^{\rm NQC}(\bar{a}_{\rm RR}) = \left(1 + \bar{a}^{\rm RR}\frac{p_{r_*}^2}{(r\Omega)^2 + \epsilon_{\rm RR}}\right)^{-1}. \qquad (9)$$

This factor was introduced in Refs. [18,22] (see also Ref. [17]). We fix the value of $\epsilon_{\rm RR}$ to $\epsilon_{\rm RR} = 0.2$ as in [22].

(iii) We use *improved "post-post-circular"* EOB dynamical initial data (positions and momenta) as in [21,22].

(iv) We use the *resummed* 3^{+2}PN accurate "inspiral-plus-plunge" Zerilli-Moncrief normalized metric waveform introduced in Refs. [18,21]. It has the form

$$\Psi_{22}^{\rm insplunge}(a, b; \nu, t) = -4\sqrt{\frac{\pi}{30}}\nu(r_\omega\Omega)^2 f_{22}^{\rm NQC}(a, b) \times F_{22}(\nu)e^{-2i\Phi}. \qquad (10)$$

Here $\Phi(t)$ is the EOB orbital phase, $\Omega = \dot{\Phi}$ is the EOB orbital frequency, $r_\omega \equiv r[\psi(r, p_\varphi)]^{1/3}$ is a modified EOB radius, with ψ being defined as

$$\psi(r, p_\varphi) = \frac{2}{r^2}\left(\frac{dA(r)}{dr}\right)^{-1} \times \left[1 + 2\nu\left(\sqrt{A(r)\left(1 + \frac{p_\varphi^2}{r^2}\right)} - 1\right)\right], \qquad (11)$$

which generalizes the 2PN-accurate Eq. (22) of Ref. [26]. The factor F_{22} is a resummed, 3^{+2}-PN-

---

[9]In the notation introduced in Sec. III below, the dominant mode corresponds to the labels $(\pm, \ell, \ell', m, n) = (+, 2, 2, 2, 0)$.

[10]Except when said otherwise, we henceforth systematically scale dimensionful quantities by means of the total rest mass $M \equiv m_1 + m_2$ of the binary system. For instance, we use the dimensionless EOB radial coordinate $r \equiv R_{\rm EOB}/M$, with $G = 1$. Note also that $\nu \equiv \mu/M$ with $\mu \equiv m_1 m_2/M$.

accurate complex amplitude correction valid during the (adiabatic) inspiral (see [21]), and $f_{22}^{\text{NQC}}(a, b)$ is the following extra complex correcting factor, aimed at taking care (in an effective way) of various non-quasicircular effects during the plunge

$$f_{22}^{\text{NQC}}(a, b) = \left[1 + a\frac{p_{r_*}^2}{(r\Omega)^2 + \epsilon_a}\right]e^{\mathrm{i}b(p_{r_*}/r\Omega)}, \quad (12)$$

where p_{r_*} is the momentum conjugate to the EOB-tortoise radial coordinate r_*. Here we shall fix $\epsilon_a = 0.12$. In these equations, we have only indicated the *explicit* appearance of the waveform flexibility parameters (a, b). In addition, the waveform is, evidently, implicitly depending on a_5, which enters the Hamiltonian, as well as on v_{pole} and $\bar{a}_{\text{RR}}$, that enter the radiation-reaction force.

(v) We use a *ring-down waveform*,

$$\Psi_{22}^{\text{ring-down}}(t) = \sum_N C_N^+ e^{-\sigma_N^+ t}, \quad (13)$$

where the label N actually refers to a set of indices (ℓ, ℓ', m, n), with $(\ell, m) = (2, 2)$ being the Schwarzschild-background multipolarity degrees of the considered $\Psi_{\ell m}$ waveform with $n = 0, 1, 2, \ldots$ being the "overtone number" of the considered Kerr-background quasinormal mode (QNM; $n = 0$ denoting the fundamental mode), and ℓ' the degree of its associated spheroidal harmonics $S_{\ell' m}(a\sigma, \theta)$. In addition $\sigma_N^+ = \alpha_N^+ + \mathrm{i}\omega_N^+$ refers to the positive complex QNM frequencies ($\alpha_N^+ > 0$ and $\omega_N^+ > 0$ indicate the inverse damping time and the oscillation frequency of each mode, respectively). The sum over ℓ' comes from the fact that an ordinary spherical harmonics $Y_{\ell m}(\theta, \phi)$ (used as expansion basis to define $\Psi_{\ell m}$) can be expanded in the spheroidal harmonics $S_{\ell' m}(a\sigma, \theta)e^{\mathrm{i}m\phi}$ characterizing the angular dependence of the Kerr-background QNMs [64]. As explained in Sec. III of Ref. [22], we use five positive-frequency QNMs computed starting from the values of $M_{\text{f}}^{\text{ring}}/M$ and $j_{\text{f}}^{\text{ring}}$ listed in Table I.

(vi) We *match* the inspiral-plus-plunge waveform to the ring-down one, on a $(2p + 1)$-tooth comb $(t_m - p\delta, t_m - (p - 1)\delta, \ldots, t_m - \delta, t_m, t_m + \delta, \ldots, t_m + p\delta)$, of total length $\Delta t = 2p\delta$, which is centered around some "matching" time t_m. We fix the integer p to the value $p = 2$, corresponding to five matching points. As mentioned above, we follow previous work [2,22,23] in fixing the "matching time" t_m to coincide with the so-called "EOB light-ring", i.e. the instant when the orbital frequency $\Omega(t)$ reaches its maximum (this defines, within the EOB approach, the merger time). As in [22], we fix $\delta = 1.7 M_{\text{f}}^{\text{ring}}$, which corresponds to a total width for the matching interval $\Delta t = 4\delta = 6.8 M_{\text{f}}^{\text{ring}}$.

(vii) Finally, we define the complete EOB matched waveform (from $t = -\infty$ to $t = +\infty$) as

$$\begin{aligned}&\Psi_{22}^{\text{EOB}}(a_5, v_{\text{pole}}, \bar{a}_{\text{RR}}, a, b, t_m, \delta; \nu, t)\\&\equiv \theta(t_m - t)\Psi_{22}^{\text{insplunge}}(t) + \theta(t - t_m)\Psi_{22}^{\text{ring-down}}(t),\end{aligned}$$
$$(14)$$

where $\theta(t)$ denotes Heaviside's step function. This *metric* EOB waveform then defines a corresponding *curvature* waveform, simply (modulo a factor r and normalization conventions) by taking two time derivatives of (14), namely

$$r\psi_4^{\ell m} = \frac{d^2}{dt^2}(rh_{\ell m}) = N_\ell\frac{d^2}{dt^2}(\Psi_{\ell m}), \quad (15)$$

where $N_\ell \equiv \sqrt{(\ell + 2)(\ell + 1)\ell(\ell - 1)}$ (see Appendix A). Note, however, that in view of the imperfect smoothness[11] of the EOB matched metric waveform (14) around $t = t_m$, we find it more convenient, when comparing EOB to numerical data that include the merger, to work with the metric waveform without taking any further time derivatives. We discuss in Appendix A the procedure that we use to compute from the numerical relativity curvature waveform a corresponding metric waveform by two time integrations.

Fixing the *a* and *b* flexibility parameters

In this brief subsection we discuss a rationale for choosing two of the EOB flexibility parameters mentioned above, namely a and b, that enter the NQC waveform correction factor (12).

Reference [18] found that it was near optimal to fix the NQC parameter a entering the modulus of the waveform[12] so as to ensure that the maximum of the modulus of the EOB quadrupolar metric waveform sits on top of that of the EOB orbital frequency, i.e., at the "EOB light-ring."[13] We shall therefore "analytically" determine the value of the waveform NQC parameter a, as a function of the symmet-

---

[11]A partial cure to this problem would consist in replacing the discontinuous step function $\theta(t - t_m)$ in Eq. (14) by one of Laurent Schwartz's well-known smoothed step functions (or "partitions of unity") $\theta_\varepsilon((t - t_m)/(2p\delta))$.

[12]Here a and b denote the parameters called a' and b' in footnote 9 of .

[13]Note that this coincidence in the locations of the maximum of $|h_{22}(t)|$ and of Ω is automatically ensured when one uses (as advocated in [2]) a "restricted" EOB waveform $\Psi_{22}(t) \propto \Omega^{2/3}\exp[-2\mathrm{i}\Phi(t)]$. It is, however, a nontrivial fact that NR results show (both in the test-mass limit [18] and in the equal-mass case [22]) that the maximum of $|\Psi_{22}(t)|$ does occur very near the maximum of the (corresponding, best matched during inspiral) EOB orbital frequency $\Omega(t)$. This can be considered as another successful prediction of the EOB formalism. Note that this property does not apply to the maximum of the modulus of other GW quantities, such as the instantaneous energy flux or the modulus of quadrupole *curvature* waveform $r\psi_4^{22}(t)$, which occur significantly after the EOB light-ring [23].

ric mass ratio $\nu = \mu/M = m_1 m_2/(m_1 + m_2)^2$ by imposing the following *requirement*: that the maximum of $|\Psi_{22}^{\text{EOB}}(t)|$ be on top of the $\Omega(t)$.

In principle, the determination of a by this requirement depends on the choice of the other EOB flexibility parameters. In other words, the satisfaction of this condition will determine a as a function of all the parameters entering the EOB dynamics and inspiral waveform: $a = a(a_5, \bar{a}_{\text{RR}}, v_{\text{pole}}, \nu)$. In practice, however, and as a first step towards a fully consistent choice of all the EOB flexibility parameters, we fixed a in the following way. In previous work it was found both analytically (when $\nu \ll 1$, see Ref. [18]) and numerically (when $\nu = 1/4$, see Ref. [22]) that the value $a = 0.5$, together with $\epsilon_a = 0.12$, led to a sufficiently accurate solution of the above requirement. For the present work, we partially took into account the parameter dependence of a by fixing $(a_5, v_{\text{pole}}, \bar{a}_{\text{RR}})$ to the central best-fit values that we will select below and by then numerically finding the optimal value of a as a function of ν only. In particular, we identified the following pairs (ν, a) of near-optimal values: (0.25, 0.44), (0.2222, 0.49), (0.16, 0.64), (0.05, 0.905), and (0.01, 0.985). These are the values that we shall use in this work. Note also that the ν-dependence can be approximately represented by a simple linear fit, namely $a(\nu) = 1.019 - 2.345\nu$.

As for the NQC parameter b entering the phase of the (quadrupolar) waveform, previous work [22] has found that it had a very small effect (when using the new, 3^{+2}-PN accurate EOB waveform which already includes the leading NQC phase correction) and that it could simply be set to $b = 0$. We shall also do so here.

IV. SELECTING BEST-FIT EOB FLEXIBILITY PARAMETERS

As recalled in the introduction, and in the previous section, the only EOB flexibility parameters whose best-fit values are still quite indeterminate are a_5, v_{pole}, and $\bar{a}_{\text{RR}}$. In this section we shall show how to remedy this situation by combining information coming from various NR data, namely, on the one hand, from published Caltech-Cornell data, and, on the other hand, from recently computed Jena data (reported here).

A. Using Caltech-Cornell published data to determine v_{pole} and $\bar{a}_{\text{RR}}$ as functions of a_5

To start with, let us recall that Ref. [21] had fixed $\bar{a}_{\text{RR}} = 0$ and had then showed that imposing one constraint relating the EOB waveform and Caltech-Cornell *inspiral* data, namely $\rho_{\omega_4}^{\text{bwd}}(a_5, v_{\text{pole}}) = 1$, (see Eq. (35) in [21]), implied a rather precise functional relationship between v_{pole} and a_5 (see Fig. 3 there). More recently, Ref. [22] compared the same type of EOB waveform with NR waveforms, computed with the CCATIE code of the Albert Einstein
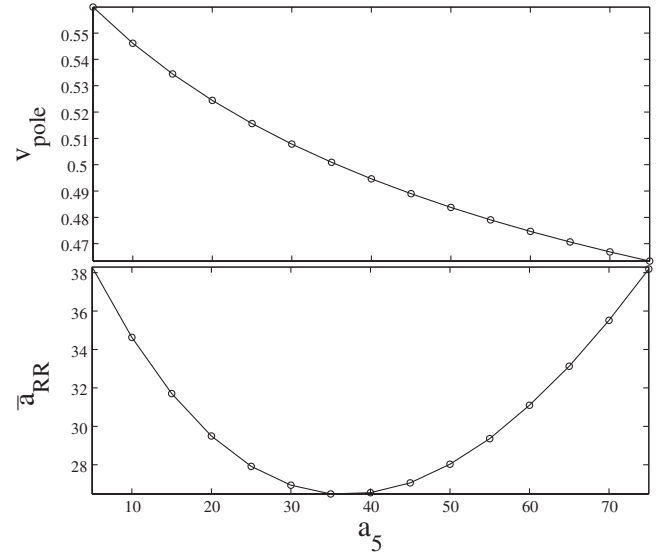

FIG. 3. Functional relationships linking v_{pole} and $\bar{a}_{\text{RR}}$ to a_5 obtained by imposing the two constraints (16) and (17) based on published Caltech-Cornell *inspiral* waveform data.

Institute, and suggested that it might be useful to flex the EOB waveform by introducing a nonzero value of $\bar{a}_{\text{RR}}$, i.e. a nonquasicircular correcting factor f^{NQC}, Eq. (9), in the radiation reaction. Here we shall combine these two strategies by starting from an EOB waveform depending on the three *a priori* independent parameters $(a_5, v_{\text{pole}}, \bar{a}_{\text{RR}})$ and by imposing *two independent constraints* relating the EOB waveform to published Caltech-Cornell data. These constraints have the form

$$\rho_{\omega_4}^{\delta t_{\omega_4}}(a_5, \bar{a}_{\text{RR}}, v_{\text{pole}}) = 1, \tag{16}$$

$$\rho_{\omega_4}^{\delta t'_{\omega_4}}(a_5, \bar{a}_{\text{RR}}, v_{\text{pole}}) = 1, \tag{17}$$

where

$$\rho_{\omega_m}^{\delta t_{\omega_m}}(a_5, \bar{a}_{\text{RR}}, v_{\text{pole}}) \equiv \frac{\Delta^{\omega_m}\phi_{\text{T4EOB}}(t_{\text{NR}}^{\omega_m} + \delta t_{\omega_m})}{\delta_m}. \tag{18}$$

Here $\Delta^{\omega_m}\phi_{\text{T4EOB}}(t_{\text{NR}}^{\omega_m} + \delta t_{\omega_m})$ is the value at the time $t_{\text{NR}}^{\omega_m} + \delta t_{\omega_m}$ of the *curvature* waveform (ψ_4^{22}) phase difference between T4 and EOB when the two waveforms are matched at the gravitational wave frequency ω_m (in the sense of [28]). The δ_m's appearing in Eq. (18) are estimates of the value of the phase difference between TaylorT4 and Caltech-Cornell numerical relativity data at various times differing from the matching time $t_{\text{NR}}^{\omega_m}$ by δt_{ω_m}, as measured by us on the left panel of Fig. 19 of [28]. Following the procedure outlined in Sec. IV of [21], we use the matching frequency $\omega_4 \equiv \omega_m = 0.1$. Then, we consider two of the measured values which have been used to produce the empty circles appearing in Fig. 5 of [21]. These two values are

$$\delta_4 = 0.055 \quad \text{corresponding to } \delta t_{\omega_4} = -1809M, \quad (19)$$

$$\delta'_4 = 0.04 \quad \text{corresponding to } \delta t'_{\omega_4} = -529M. \quad (20)$$

The data point $(\delta t_{\omega_4}, \delta_4)$ corresponds to the leftmost empty circle on the top panel of Fig. 5 of [21], while the point $(\delta t'_{\omega_4}, \delta'_4)$ corresponds to the next-to-next empty circle on the right of $(\delta t_{\omega_4}, \delta_4)$. The former data point was used in Ref. [21] as the "main backward" ω_4 data. Note that the new data point that we use here is also "backward" (with respect to $\omega_m = \omega_4 = 0.1$), though it is less backward by about a factor three. We use these two points here because we think they represent the best "lever arms" to exploit the approximate[14] numerical data represented in Fig. 5 of [21]. In particular, we do not use any "forward" data point because the accuracy with which we could measure them is more uncertain. Let us emphasize that, as a consequence of this choice, our determination of the functional relationships $v_{\text{pole}}(a_5)$ and $\bar{a}_{\text{RR}}(a_5)$ exhibited below only relies on Caltech-Cornell data up to gravitational wave frequency $M\omega \lesssim 0.1$.

The two constraints (16) and (17) were solved by numerical Newton-Raphson iteration in v_{pole} starting from a grid of values of $(\bar{a}_{\text{RR}}, a_5)$. The iteration was stopped when the constraints were satisfied to better than the 10^{-4} level. The result of this procedure consists of two separate functional relations linking, on the one hand, v_{pole} to a_5 and, on the other hand, $\bar{a}_{\text{RR}}$ to a_5. These two functional relations are plotted in Fig. 3. The upper panel of the figure is a modified version of the $v_{\text{pole}}(a_5)$ functional relationship represented in the upper panel of Fig. 3 of [21]. The latter curve was drawn by fixing $\bar{a}_{\text{RR}}$ to zero and by imposing only the first constraint, $\rho_{\omega_4}^{\delta t_{\omega_4}}(a_5, 0, v_{\text{pole}}) = 1$. By contrast, the curve $v_{\text{pole}}(a_5)$ in the upper panel of Fig. 3 was obtained by *simultaneously* tuning v_{pole} and $\bar{a}_{\text{RR}}$ so as to satisfy the *two* constraints (16) and (17). The numerical data behind the plots of Fig. 3 are also given in explicit numerical form in Table II. [The many digits quoted there are only given for comparison purposes.]

In the upper panel of Fig. 4 we exhibit, for the particular value $a_5 = 25$ (and, correspondingly, $\bar{a}_{\text{RR}} = 27.9197$ and $v_{\text{pole}} = 0.515\,63$) the near-perfect agreement between the two ω_4-*matched* phase differences $\phi_{\text{T4}} - \phi_{\text{EOB}}$ and $\phi_{\text{T4}} - \phi_{\text{NR}}$. [Our choice of the particular value $a_5 = 25$ will be motivated in the next subsection]. For completeness, we have also included in the upper panel (see dash and dash-dot curves) the analogous phase differences

---

[14]As a measure of the accuracy of the approximate data points quoted in Eqs. (19) and (20) above, let us mention that we have, since, directly determined from the Caltech-Cornell numerical data provided to us the values $\delta_4 = 0.054\,97$ corresponding to $\delta t_{\omega_4} = -1809M$, and $\delta'_4 = 0.039\,57$ corresponding to $\delta t'_{\omega_4} = -529M$ (with a numerical relativity time $t_{\omega_4} = 3782.1489M$ corresponding to $\omega_4 = 0.1$).

TABLE II. Explicit values of the EOB effective parameters $\bar{a}_{\text{RR}}$ and v_{pole} for a certain sample of a_5. These values correspond to imposing the two constraints $\rho_{\omega_4}^{\delta t'_{\omega_4}} \simeq 1 \pm 10^{-4} \simeq \rho_{\omega_4}^{\delta t_{\omega_4}}$.

a_5	$\bar{a}_{\text{RR}}$	v_{pole}
5.0000	38.286 713 287	0.559 878 668
10.0000	34.630 281 690	0.546 122 851
15.0000	31.708 633 094	0.534 478 193
20.0000	29.496 402 878	0.524 422 704
25.0000	27.919 708 029	0.515 629 404
30.0000	26.940 298 507	0.507 845 655
35.0000	26.484 962 406	0.500 903 097
40.0000	26.545 801 527	0.494 646 066
45.0000	27.057 692 308	0.488 978 922
50.0000	28.031 496 063	0.483 798 488
55.0000	29.360 000 000	0.479 064 301
60.0000	31.097 560 976	0.474 690 707
65.0000	33.130 252 101	0.470 660 186
70.0000	35.517 241 379	0.466 908 044
75.0000	38.189 655 172	0.463 416 027

matched at the matching frequencies $\omega_2 = 0.05$ and $\omega_3 = 0.063$ instead of $\omega_4 = 0.1$. The visual agreement between these three phase-difference curves and the corresponding ones displayed in the left panel of Fig. 19 in Ref. [28] is striking. [As in Fig. 19 of [28], we use here TaylorT4 3.5/2.5; see Appendix B for its precise definition]. The lower panel of Fig. 4 plots the ω_4-matched phase difference $\phi_{\text{EOB}} - \phi_{\text{NR}} = [\phi_{\text{T4}} - \phi_{\text{NR}}] - [\phi_{\text{T4}} - \phi_{\text{EOB}}]$, i.e.,
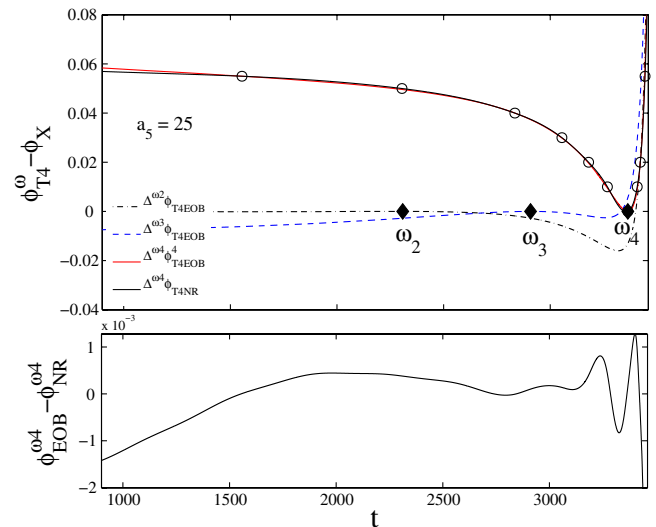

FIG. 4 (color online). Top panel: near-perfect agreement between T4-EOB and T4-NR phase differences when $a_5 = 25$, $\bar{a}_{\text{RR}} = 27.9197$, and $v_{\text{pole}} = 0.51563$. Here NR refers to the published results of the Caltech-Cornell inspiral simulation. The corresponding EOB-NR phase difference (bottom panel) is of the order of 10^{-3} radians over the 30 GW cycles of the Caltech-Cornell inspiral simulation.

the difference between the two solid curves (red online and black) in the upper panel.

Note that this phase difference varies between -0.0014 and $+0.0008$ radians over the time span of ($\sim 2464M$ up to $M\omega = 0.1$) which was used in our EOB-CC fitting procedure. A study of the continuation of the curve exhibited in the bottom panel of Fig. 4 then shows that, after $M\omega = 0.1$ and up to a final frequency $M\omega = 0.1565$, this phase difference varies between $+0.0013$ and -0.0185 radians over a time span of $96M$. Note that a recent report [60] has indicated that a refined estimate of the total phasing error in the Caltech-Cornell simulation was of the order of 0.01 radians over the entire span of the simulation. Therefore the accuracy of our EOB-fit is consistent with such an error estimate.

Summarizing so far: by best-fitting the three-parameter flexed EOB waveform $\Psi_{22}^{\text{EOB}}(a_5, v_{\text{pole}}, \bar{a}_{\text{RR}}; t)$ to published[15] Caltech-Cornell *inspiral* data before $M\omega = 0.1$ (in the sense of imposing the two constraints Eqs. (16) and (17)) we have reduced the number of independent unknown EOB flexibility parameters to only one, namely the "4 PN" EOB parameter a_5. The basic physical reason behind the difficulty of determining a_5 by means of inspiral data only (especially when relying, as we did above) on data below GW frequency 0.1, is the fact that a_5 starts significantly affecting the EOB dynamics (and waveform) only during the late-inspiral, when the dynamics becomes strongly nonadiabatic. Our next step will be to constrain a_5 by best-fitting the EOB waveform to numerical data covering more of the late-inspiral dynamics.

B. Using numerical data covering late-inspiral and plunge to constrain the "4 PN" EOB flexibility parameter a_5

In this subsection we shall fulfill, at least in first approximation, the aim of the EOB-NR comparisons initiated in Refs. [16,20–22]; i.e., to determine an essentially unique set of "best-fit" EOB flexibility parameters $(v_{\text{pole}}, \bar{a}_{\text{RR}}, a_5)$. In view of the results of the previous subsection, we now need to best-fit the *one-parameter flexed* EOB waveform

$$\Psi_{22}^{\text{EOB}}(a_5; t) \equiv \Psi_{22}^{\text{EOB}}[v_{\text{pole}}(a_5), \bar{a}_{\text{RR}}(a_5), a_5; t], \qquad (21)$$

where $v_{\text{pole}}(a_5)$ and $\bar{a}_{\text{RR}}(a_5)$ are the functional relation-

ships illustrated in Fig. 3 above, to a numerical waveform smoothly connecting, without interruption, the nonadiabatic late inspiral to the early inspiral and to the subsequent plunge. Here we shall make use of recently computed numerical data (see Sec. II) that cover (for the equal-mass case) about 20 GW cycles of inspiral and plunge up to merger. As we shall see, for the purpose of determining a_5, we will mainly use the signal only up to the plunge.

As quantitative measure of the EOB-NR agreement we shall consider here the following L_∞ norm of the a_5-dependent EOB-NR phase difference (using the EOB metric waveform, Eq. (21) above)

$$\|\Delta\phi\|_\infty^{\text{EOBNR}}(a_5; t_1, t_2; t_L, t_R) \equiv \sup_{t\in[t_L,t_R]}|\phi_{22}^{\text{EOB}}(a_5; t + \tau_{12})$$
$$+ \alpha_{12} - \phi_{22}^{\text{NR}}(t)|. \qquad (22)$$

Here $[t_L, t_R]$ denotes the time interval on which one computes the L_∞ norm of the phase difference. In addition, (t_1, t_2) denote two pinching times which are used to determine some time and phase shifts, $\tau_{12} = \tau(t_1, t_2)$ and $\alpha_{12} = \alpha(t_1, t_2)$, needed to compare the EOB and NR phase functions (which use different time scales and phase references).

Let us recall the "two-pinching-times" procedure, introduced in [22], for determining the time and phase shifts τ and α. First, the two waveforms being complex numbers, we decompose them in amplitude and phase: $\Psi_{22}^X = A_X \exp(-i\phi^X)$ where the label X can be either "EOB" or "NR." The corresponding instantaneous (metric) GW frequencies are then defined as $\omega^X(t) \equiv d\phi^X/dt$. We start by fixing two pinching times (t_1, t_2) on the NR time scale t. We then define the time shift τ by solving the equation $\phi^{\text{NR}}(t_2) - \phi^{\text{NR}}(t_1) = \phi^{\text{EOB}}(\tau + t_2) - \phi^{\text{EOB}}(\tau + t_1)$. Then, we define the phase shift α such that $\phi^{\text{NR}}(t_1) = \phi^{\text{EOB}}(t_1 + \tau) + \alpha$. In the limiting case where the corresponding GW frequencies $\omega_1 = \omega^{\text{NR}}(t_1)$ and $\omega_2 = \omega^{\text{NR}}(t_2)$ are nearly coincident, $\omega_1 \approx \omega_m \approx \omega_2$, this procedure coincides with the one introduced in Ref. [28] and based on the choice of a single matching frequency ω_m.

We shall first consider the equal-mass case, $\nu = 1/4$. For this case we choose the following NR pinching times: $t_1 = 1764.9$ and $t_2 = 1940.1$ (corresponding to NR gravitational wave frequencies $\omega_1^{22} = 0.0998$ and $\omega_2^{22} = 0.4717$). These times *bracket the merger time*. This is done to optimize the EOB-NR agreement over the physically most crucial (and possibly numerically most accurate) part of the waveform, i.e. the late-inspiral, plunge, merger, and ring-down. Concerning the choice of the interval $[t_L, t_R]$ used to compute the L_∞ norm, we selected it with the following criteria in mind: as a_5 is most important during late-inspiral and plunge, but is somewhat uncorrelated to the way EOB approximates the plunge-ring-down matching, we chose $[t_L, t_R]$ to cover the crucial stage of the late-inspiral. More precisely, we have fixed t_R such that the NR gravitational wave phase is approximately 7.6 radians (i.e. 1.21 GW cycles) smaller than the phase when the EOB

---

[15]Since we had recently access to the actual Caltech-Cornell data we could and did check the reliability of the results obtained from the published data. In particular, when computing the phase difference $\phi_{\text{EOB}} - \phi_{\text{CC}}^{\text{actual}}$ we essentially recovered the results quoted in the text. For instance, we find that the actual phase difference varies between: -0.002 radians at Caltech-Cornell time $600M$ and $-0.017\,66$ radians at the end of the simulation ($M\omega = 0.1565$), passing through zero at $M\omega = 0.1$. The number of GW cycles between $t_{\text{CC}} = 600M$ and $t_{\text{CC}} = 3782$ ($M\omega = 0.1$) is 22.10, while the number of GW cycles in the final part of the simulation (after frequency 0.1) is 2.16.

waveform modulus reaches its maximum (which is close to merger time in view of the discussion of Sec. III). Then, t_L was chosen such that $\phi^{NR}(t_L)_{22} = \phi_{22}^{NR}(t_R) - 58.5$. Their numerical values are $t_L = 1198.8M$ and $t_R = 1899.6M$, while the corresponding NR gravitational wave frequencies are $\omega_L^{22} = 0.05952$ and $\omega_R^{22} = 0.1898$, respectively. Using these specified values we have computed the L_∞ norm of the EOB-Jena phase difference, Eq. (22), as a function of a_5. The result is plotted, as a solid line (1:1 mass ratio), in Fig. 5. This figure shows that the limited range of values $20 \lesssim a_5 \lesssim 30$ is preferred in that it yields a *minimum* of the largest EOB-NR phase difference $\|\Delta\phi\|_\infty^{EOBNR}$ over the $[t_L, t_R]$ interval specified above. This minimum phase difference is on the order of 0.01 radians. We note, in passing, that this late-inspiral interval partially overlaps (frequencywise) with the range of the published Caltech-Cornell data as we used it above (i.e., focusing on frequencies $M\omega \lesssim 0.1$), but crucially extends to frequencies reaching roughly as high as the EOB adiabatic last stable orbit (LSO) frequency ($\omega_{LSO}^{EOB} = 0.2114$). Though Fig. 5 is qualitatively similar to the L_∞ norm of the EOB/Caltech-Cornell phase difference displayed in Fig. 4 of Ref. [21], it is important to remark that in the latter figure the L_∞ norm varied by only about a factor 2 over the entire a_5 range, $0 \leq a_5 \leq 100$. By contrast, in the current Fig. 5 the L_∞ norm varies by about a factor 2 in the much smaller interval $15 \leq a_5 \leq 35$ and then increases by almost a factor 10 over the entire a_5 range, $5 \leq a_5 \leq 75$. We can now use the "uncertainty level" ± 0.026 radians in $\phi_{22}^{NR} \equiv \phi_{22}^{Jena}$ (determined in Sec. II C above by comparing it with Caltech-Cornell data), as indicated by the horizontal line in the figure, to determine a corresponding interval of "best-fit" values of a_5. Though this uncertainty level is

admittedly rather uncertain at this stage, it suggests that the real[16] value of a_5 probably lies in the interval $12 \lesssim a_5 \lesssim 40$. To firm up our conclusion, we have also considered numerical data concerning the 2:1 mass-ratio case. In that case we considered again the L_∞ norm, Eq. (22), and we made similar choices both for the pinching times and for the extremities of the L_∞ interval. In particular, t_R was chosen to sit 7.6 radians before the maximum modulus while we kept the left-right phase difference to the same value as above, namely $\phi_{22}^{NR}(t_L) = \phi_{22}^{NR}(t_R) - 58.5$. The resulting $L_\infty(a_5)$ function is plotted as a dashed line in Fig. 5. Though the minimum of this curve is much more shallow than before, the important fact is that the 1:1 preferred a_5 range is consistent with the 2:1 L_∞ result. Let us observe (without wishing to attribute any deep significance to this fact) that the preferred range for a_5 happens to be close to the "special" a_5 value for which the "EOB-horizon" decreases, when ν increases up to 1/4, down to a vanishing EOB radial coordinate. Indeed the P_4^1 Padé approximant that we use here to define the a_5-flexed EOB radial potential $A(u) = P_4^1[A^{Taylor}(u)]$ has the structure $A(a_5; u) = (1 - r_H u)/D_4(u)$ where $D_4(u)$ is a 4th-order polynomial in ν (see Eq. (3.10d) of Ref. [17]), and where

$$r_H(a_5, \nu) = 4\frac{768 - (3584 - 123\pi^2)\nu - 24a_5\nu}{1536 - (3776 - 123\pi^2)\nu}. \quad (23)$$

Here r_H is the radial location of the "EOB-horizon," in the sense that $A(u)$ vanishes for $r \equiv 1/u = r_H$ (at least when r_H is positive). For any given positive a_5, r_H is a decreasing function of ν. If we require that r_H stays positive for all values of $\nu \in [0, 1/4]$, we find that a_5 must be smaller than the special value

$$a_5^* = \frac{123\pi^2 - 512}{24} = 29.2484. \quad (24)$$

Note, however, that there is nothing *a priori* wrong with higher values of a_5. In that case the radial function $A(r)$, considered versus r, has anyway a third-order zero at $r = 0$.

Summarizing: by combining the comparison of the EOB waveform with, on the one hand, published Caltech-Cornell inspiral data and, on the other hand, our coalescence data, we have been able to select a preferred small region of the EOB flexibility parameters. This region is made of (approximately) correlated triplets $[a_5, v_{pole}(a_5), \bar{a}_{RR}(a_5)]$, and is located between the second and the eighth lines of Table II.
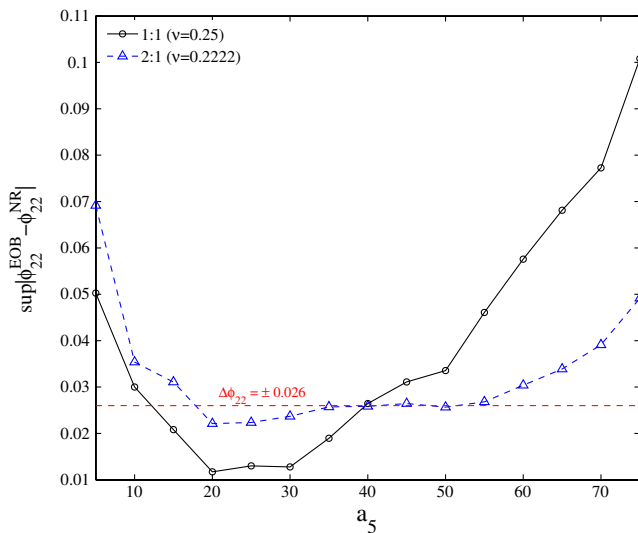

FIG. 5 (color online). L_∞ norm of the EOB-NR late-inspiral ($[t_L, t_R]$) phase difference, as a function of a_5 for $\nu = 0.25$ (1:1 mass ratio) and $\nu \simeq 0.2222$ (2:1 mass ratio). NR refers to results of Jena coalescence simulations reported here.

---

[16]Note that though a_5 is, to start with, a theoretically well-defined quantity within the EOB framework, its "experimental measurement" obtained by comparing specifically resummed versions of the EOB waveforms with numerical data partially transforms it into an "effective parameter" describing a complicated nonperturbative process.

V. DETAILED EOB-NR WAVEFORM COMPARISONS FOR $a_5 = 25$

To confirm the validity of the conclusions reached in the previous section, we shall now study in detail the performance of the center of the above-selected interval, namely $a_5 = 25$ together with the corresponding values of $\bar{a}_{\rm RR}$ and $v_{\rm pole}$ listed in Table II.

In this section we shall consider numerical waveforms for *three* different values of ν, namely $\nu = 0.25$, $\nu = 2/9 = 0.2222$, and $\nu = 0.16$ (corresponding, respectively, to the mass ratios 1:1, 2:1, and 4:1) extracted from the simulations of Table I. Note that our best-fit procedure outlined above essentially relied only on the 1:1 mass-ratio case so that the other cases that we consider here will test the ability of the EOB formalism to capture the NR waveforms. The EOB flexibility parameters used for the various mass ratios are the ones listed in the fifth row of Table II. In view of the proximity of the "best-fit" $v_{\rm pole}$ value $v_{\rm pole}^{\rm best}(\nu = 0.25) = 0.5156$ to the "best-fit" $v_{\rm pole}$ found (following the strategy of [21]), in the test-mass limit, $v_{\rm pole}^{\rm best}(\nu = 0) = 0.526\,55$ (for the P_4^4 4 PN-accurate flux), we made no attempt at interpolating $v_{\rm pole}(\nu)$ between the two values of ν.

To compare EOB and NR waveforms we follow the procedure indicated above. This procedure involves choosing two pinching times t_1 and t_2 (which should not be confused with the L_∞ times $t_{\rm L}$ and $t_{\rm R}$ which will play no role in this section). We summarize in Table III the pinching times we use, together with the corresponding frequencies. Note that in all cases the lowest pinching frequency is around 0.1 while the highest one (reached after the merger) is roughly 10% lower than the main ring-down frequency.

The results of the detailed EOB-NR comparison are presented in Figs. 6 and 7. For completeness, we have used the full numerical waveforms including the burst of junk radiation it contains at the beginning.

The two upper panels of Fig. 6 refer to the equal-mass case ($\nu = 0.25$). On the left, we plot the "pinched" EOB-NR phase difference (in radians) over the full simulation time (see inset). Note that the total simulation covers about ~ 146 radians of the GW phase; i.e., 23.24 GW cycles (starting from the beginning of the inspiral, when $t_{\rm NR} \sim 110M$, to the middle of the ring-down, up to $t_{\rm NR} = 1980M$). We see that the EOB-NR phase disagreement stays quite small during most of the inspiral. More pre-

TABLE III. Pinching NR times and corresponding NR gravitational wave frequencies used to perform the EOB-NR comparison of Fig. 6.

ν	t_1	t_2	ω_1^{22}	ω_2^{22}
0.25	1764.9	1940.1	0.0998	0.4716
0.2222	893.9	1071.9	0.1005	0.4542
0.16	1297.6	1476.3	0.1051	0.4189

cisely $\Delta\phi^{\rm EOBNR}$ stays in the range $[-0.04, 0.01]$ all over the time interval $1200 \lesssim t_{\rm NR} \lesssim 1930$. This corresponds to a "two-sided" (in the sense of footnote 12 of Ref. [22]) EOB-NR phase difference smaller than ± 0.025 radians, or ± 0.004 GW cycles over $730M$. As in a previous analysis, the jump in the phase difference around $t_{\rm NR} \approx 1930$ is connected to the rather coarse way in which the EOB formalism represents the merger. Still, the accumulated phase difference over the transition between plunge and ring-down is only of the order of 0.15 radians; i.e., 0.02 GW cycles. Note that over the full simulation time (see inset in top-left panel) there is an accumulated phase difference of about -0.2 radians. In view of the discussion on the accuracy of the numerical simulations in Sec. II, it is quite possible that this difference is mainly due to effects related to the use of finite extraction radii. Similarly, part of the phase disagreement around the merger might come from numerical inaccuracies. The upper-right panel of the figure compares the real part of the two metric waveforms. The visual agreement between the two is striking, apart from the amplitude disagreement ($\sim 20\%$, see below) localized around the merger. In view of the discussion in Sec. II, part of this difference might also have a numerical origin.

The bottom panels of Fig. 6 refer to the 2:1 mass-ratio case ($\nu = 2/9 = 0.2222$). Here the phase agreement (left panel) is even better than before. Over the nearly full time interval $143 \lesssim t_{\rm NR} \lesssim 1100$ the EOB-NR (two-sided) phase difference is smaller than ± 0.05 radians; i.e., ± 0.008 GW cycles. The corresponding middle-right panel compares the real part of the two metric waveforms. Again, the agreement is striking apart from a $\sim 20\%$ amplitude disagreement localized around the merger (see below).

Finally, Fig. 7 deals with the 4:1 mass-ratio case ($\nu = 0.16$). Here the agreement is still quite good, though it is noticeably less good than in previous cases. Consistently with the discussion of numerical accuracy in Sec. II, this less compelling accordance is likely to have its origin in numerical discretization errors. A clarification of this issue would need higher-accuracy simulations.

Figure 8 completes the comparison between EOB and NR waveforms, for the equal-mass-ratio case, by simultaneously displaying, versus time: (i) the two GW frequencies,[17] (ii) twice the EOB orbital frequency Ω, and (iii) the two moduli. The leftmost (dashed) vertical line indicates the location of the EOB adiabatic LSO, while the rightmost one refers to the "EOB-light-ring." Though this figure exhibits the approximate nature of the EOB-matching procedure (notably visible in the small differences in the GW frequencies), it also illustrates how the apparently coarse EOB-matching procedure is able to effectively re-

---

[17]For clarity we add in several figures a subscript 22 to the gravitational wave frequency or phase as a reminder of the fact that we compare quadrupolar $\ell = m = 2$ waveforms.
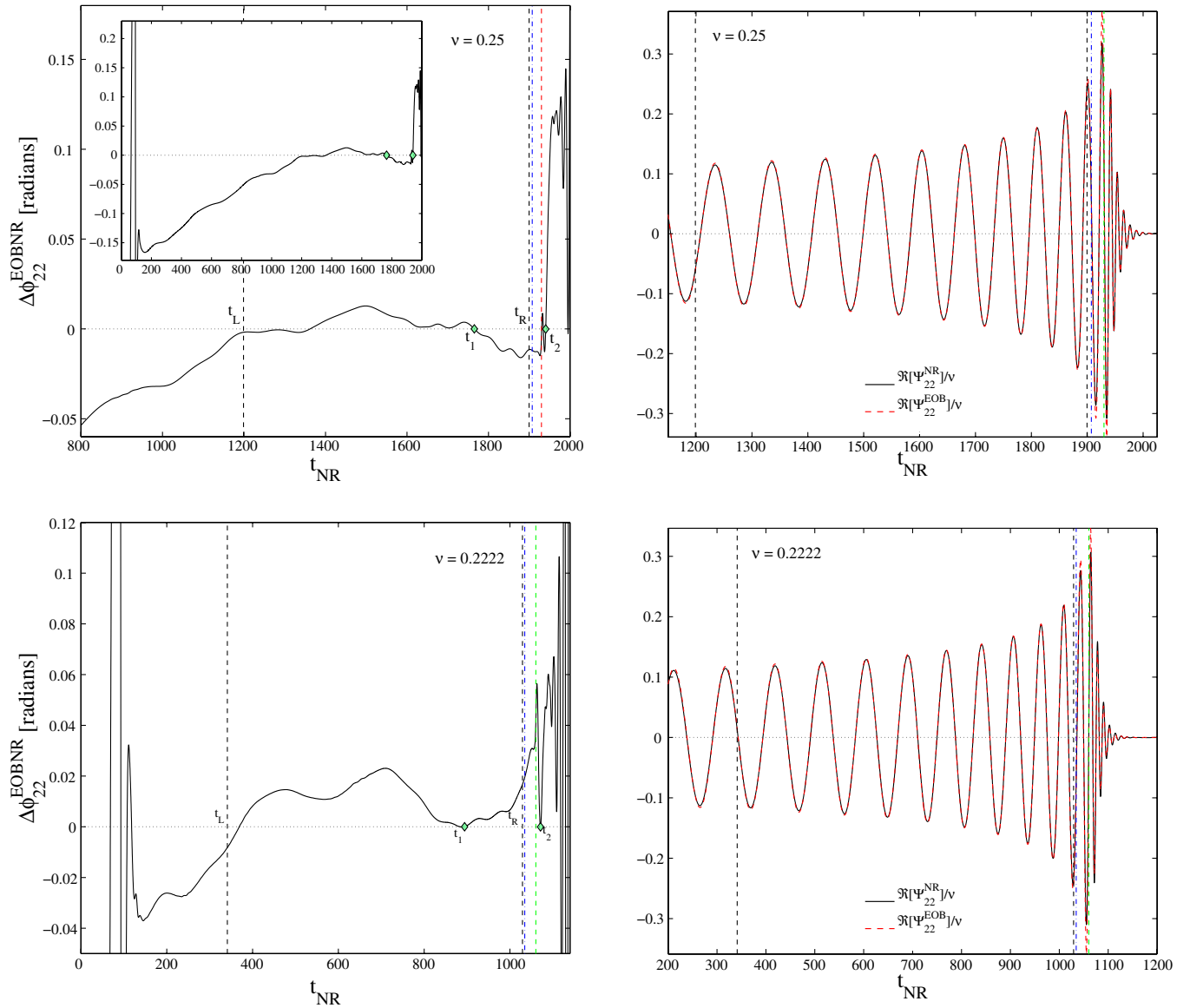
FIG. 6 (color online). Comparison between NR and EOB waveforms for $\nu = 0.25$ (top), $\nu = 0.2222$ (bottom). The left panels depict the EOB-NR phase difference; the right panels show the real part of the metric waveforms. Here, NR refers to the full results of Jena coalescence simulations, from early inspiral to ring-down, by contrast to the L_∞ norm of Fig. 5 which concerned a late-inspiral stage $[t_L, t_R]$. This interval is indicated on the figures. The pinching times (t_1, t_2) of Table III are also shown. The dash-dot and the dash vertical lines at the extreme right of the figures mark the location of the EOB adiabatic LSO and the "EOB light-ring," respectively.

produce, with high accuracy, the overall time variation of the GW frequency through the merger onto the ring-down. We have obtained similarly good agreements for the other mass ratios.

We conclude this section by showing in Fig. 9 the fractional amplitude differences, for the three mass ratios considered here, between EOB and NR waveforms. The solid line in the figure plots the quantity $\Delta A/A \equiv (A_{\rm EOB} - A_{\rm NR})/A_{\rm NR}$ versus NR time for $\nu = 0.25$. It is quite possible that the approximately linear trend visible on this (solid) line is due to effects related to the finite-extraction radius; the decrease in amplitude disagreement as we go to later

inspiral times is consistent with the decrease in amplitude uncertainty (as discussed in Sec. II) as the amplitude rises. If this is the case, the minimum value, before the merger, might be indicative of the actual EOB-NR amplitude agreement. For $\nu = 0.25$ this minimum is $\min[\Delta A/A] \approx +5 \times 10^{-3}$. The jump in $\Delta A/A$ during merger is of the order of 20%. Though part of this jump might have a numerical origin, we think that most of it comes from the EOB approximate matching procedure around merger. Let us recall, in this respect, that in Ref. [22] $\Delta A/A$, for $\nu = 0.25$, was of order $\pm 1\%$ during inspiral and rose to a maximum of $+18\%$ at merger. The leftmost curve (dashed
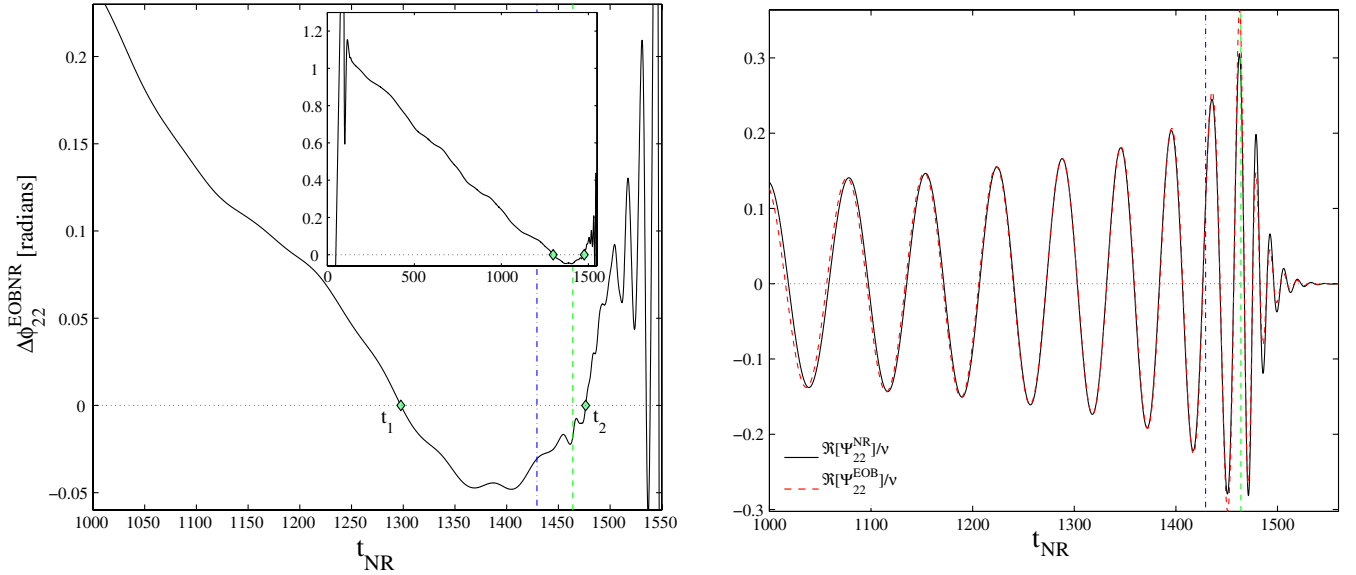
FIG. 7 (color online). Comparison between NR and EOB waveforms for $\nu = 0.16$. The left panel depicts the EOB-NR phase difference; the right panels show the real part of the metric waveforms. The pinching times (t_1, t_2) of Table III are also shown. The dash-dot and the dash vertical lines at the extreme right of the figures mark the location of the EOB adiabatic LSO and the "EOB light-ring," respectively.

line) on Fig. 9 refers to the $\nu = 0.2222$ case, while the middle curve (dash-dot line) refers to the $\nu = 0.16$ case. For the same reasons as above it is likely that the approximate linear trends (which are smaller by a factor ~ 2 than before) are of numerical origin. The minimum values

before merger of $\Delta A/A$ are $\min[\Delta A/A] \approx +7 \times 10^{-3}$ (for $\nu = 0.2222$) and $\min[\Delta A/A] \approx +5 \times 10^{-3}$ (for $\nu = 0.16$). Note that the jumps in $[\Delta A/A]$ around merger are quite similar to the $\nu = 0.25$ case, namely, about $\sim +20\%$.

VI. CONCLUSIONS

We have compared the "flexed" [17,18] resummed 3^{+2}PN-accurate [21] EOB waveform to two, independent,
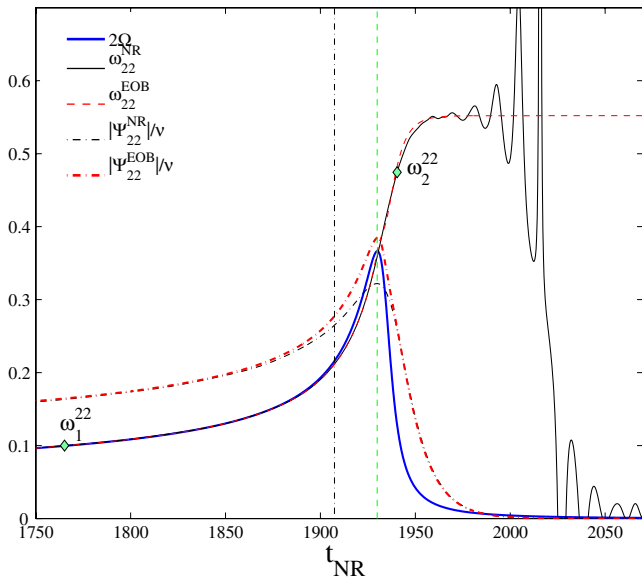
FIG. 8 (color online). Comparison between EOB and NR instantaneous gravitational wave frequencies (and moduli) for the equal-mass case, $\nu = 0.25$. Here, as in Fig. 9, NR refers to the Jena coalescence simulation. The dash-dot vertical line indicates the EOB adiabatic LSO, while the dash one indicates the "EOB light-ring." The pinching frequencies $(\omega_1^{22}, \omega_2^{22})$ of Table III are also indicated.
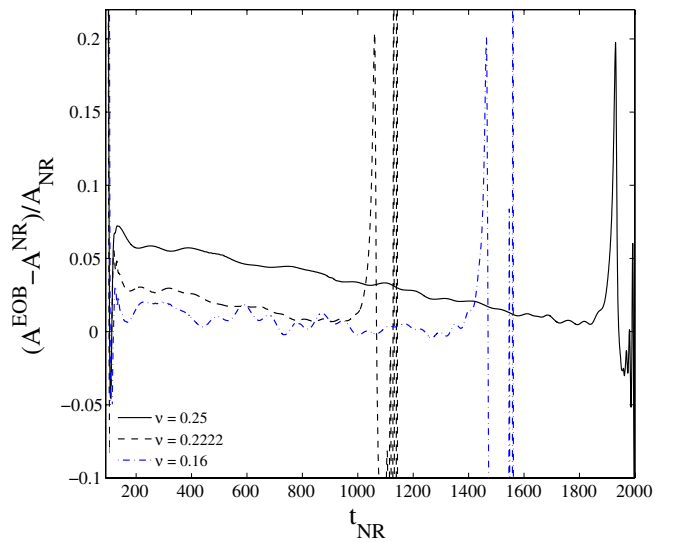

FIG. 9 (color online). Fractional EOB-NR differences in the gravtitational wave (metric) amplitudes, $A \equiv |\Psi_{22}|$, versus NR time for different mass ratios.

NR data on inspiralling and/or coalescing binary black-hole systems: on the one hand, published Caltech-Cornell *inspiral* data [28] (mainly used by us only up to $M\omega \lesssim 0.1$) and, on the other hand, newly computed *coalescence* data using the BAM code [30,31].

We effected this EOB-NR comparison with a strategy allowing us to locate a "best-fit spot" in the space of the three main EOB flexibility parameters $(a_5, v_{\mathrm{pole}}, \bar{a}_{\mathrm{RR}})$. This strategy is multipronged:

(i) We selected two measurements of published Caltech-Cornell equal-mass inspiral data concerning the TaylorT4-NR phase differences at two different times, approximately spanning the GW frequency interval $0.04 \lesssim \omega \lesssim 0.1$.

(ii) We imposed two constraints requiring that these NR phase differences be equal to two corresponding analytical TaylorT4-EOB phase differences, see Eqs. (16) and (17). This gave us two equations for the three main flexibility parameters $(a_5, v_{\mathrm{pole}}, \bar{a}_{\mathrm{RR}})$. By numerically solving these two equations we determined two functional relationships linking, separately, v_{pole} to a_5 and $\bar{a}_{\mathrm{RR}}$ to a_5. See Fig. 3 and Table II.

(iii) Having in hand these "Caltech-Cornell-preferred" functional relationships $v_{\mathrm{pole}}(a_5)$ and $\bar{a}_{\mathrm{RR}}(a_5)$, we selected from our newly computed coalescence simulation (again for the equal-mass case[18]) a time interval $[t_L, t_R]$ corresponding to the following GW frequency interval $0.060 \lesssim \omega \lesssim 0.19$. On this time interval we compared the Jena numerically simulated phase evolution to the a_5-dependent analytical EOB one, and we computed the L_∞ norm of their difference, i.e. [see Eq. (22) for more details]

$$\|\Delta\phi\|_\infty^{\mathrm{EOBNR}}(a_5; t_L, t_R) \equiv \sup_{t \in [t_L, t_R]}$$
$$\times |\phi_{22}^{\mathrm{EOB}}(a_5; t) - \phi_{22}^{\mathrm{NR}}(t)|. \tag{25}$$

(iv) We plotted (as a solid line) in Fig. 5 $\|\Delta\phi\|_\infty^{\mathrm{EOBNR}}$ as a function of a_5. We found that this L_∞ norm has a rather well localized minimum around the region $20 \lesssim a_5 \lesssim 30$. To transform this fact into an actual "error-bar" on the value of a_5 we would need to have in hand a precise measure of the level of the errors present in the (Jena) numerical data over the time interval $[t_L, t_R]$ on which the L_∞ norm is computed. At this stage we do not have at our disposal a reliable measure of this error. However, in Sec. II C we have given what we think is our current best estimate of this error level by directly comparing, on the crucial time interval $[t_L, t_R]$, the Jena phase

data to the actual Caltech-Cornell data. This current best estimate is ± 0.026 radians and, according to Fig. 5, would correspond to the following confidence interval for a_5: $12 \lesssim a_5 \lesssim 40$. More work is needed to nail down in a more precise way the error level in the Jena phase (see, in particular, our discussion above on the internal error estimate based on comparing various radius extrapolations methods). In addition, for any value of a_5 in such an allowed confidence level, we would conclude that the corresponding triplets of correlated values a_5, $v_{\mathrm{pole}}(a_5)$, and $\bar{a}_{\mathrm{RR}}(a5)$ obtained from Table II, determine preferred best-fit values of the EOB flexibility parameters[19] $(a_5, v_{\mathrm{pole}}, \bar{a}_{\mathrm{RR}})$. In other words, our current preferred values of the EOB parameters $(a_5, v_{\mathrm{pole}}, \bar{a}_{\mathrm{RR}})$ lie between the second an the eighth lines of Table II.

(v) The present implementation of this strategy is, however, certainly somewhat affected by numerical noise. A possible indication of this fact is that the computation of a similarly selected L_∞ norm pertaining to the 2:1 mass-ratio simulation gives results (plotted as a dashed line in Fig. 5) which, though they are fully consistent with the 1:1 mass-ratio case, exhibit a more shallow minimum versus a_5. For the 2:1 L_∞ diagnostic to select an interval of preferred values of a_5 we would need a reliable estimate of the numerical error level in the 2:1 phase data. However, at this stage we do not have such an estimate. The rough error level quoted in Sec. II D is just a very conservative upper limit which, moreover, does not concern the specific time interval $[t_L, t_R]$ we are interested in. Let us emphasize that, anyway, even if a_5 is allowed to vary in the full interval $5 \lesssim a_5 \lesssim 75$ that we explored, the maximum EOB-NR phase disagreement (on the considered late-inspiral interval, which corresponds to about 58.5 radians before crossing the last stable orbit) is below 0.1 radians, i.e. 0.015 GW cycles.

(vi) We think that it would be necessary to devote a special effort toward having very high-accuracy numerical simulations covering the crucial late-inspiral, corresponding to the frequency range $0.1 \lesssim \omega \lesssim 0.2$, for several mass ratios. Pending the availability of such simulations, we provisionally conclude that our current "best-bet" choice of EOB flexibility parameters is at the center of the above-selected interval; i.e., it is given by $a_5 \simeq 25$ together with the correlated values of v_{pole} and $\bar{a}_{\mathrm{RR}}$ listed in Table II. In Sec. V we presented evidence that these

---

[18]When best-fitting the EOB flexibility parameters, we use $\nu = 0.25$ data because these are more sensitive to a_5.

[19]Note that the functional relationships $v_{\mathrm{pole}}(a_5)$ and $\bar{a}_{\mathrm{RR}}(a_5)$ discussed above have no invariant physical meaning and are just intermediate tools in converging on the looked-for best-fit point in the three-dimensional EOB flexibility parameter space.

values of $(a_5, v_{pole}, \bar{a}_{RR})$ lead to an excellent agreement between EOB and NR for several mass ratios and for the entire time interval covering inspiral, late-inspiral, plunge, merger, and ring-down. In particular, we found that the dephasing between EOB and our new coalescence data are smaller than: (i) $\pm 4 \times 10^{-3}$ GW cycles over $730M$ (11 cycles), in the equal-mass case, and (ii) $\pm 8 \times 10^{-3}$ GW cycles over about $900M$ (17 cycles) in the 2:1 mass-ratio case. In addition, we recall that the phase difference between our current "best-bet" EOB and both *published* and *actual* Caltech-Cornell data stays within 0.018 radians over the entire span of the simulation. Such a phase inaccuracy is comparable with the current, updated estimate of the numerical errors of the waveforms of Ref. [28], namely, 0.01 radians [60].

As a contrast to the EOB performance, we also study in Appendix B the performance of the TaylorT4 approximant. Our analysis shows that the apparently good performance of TaylorT4 during the inspiral is due to a lucky compensation between two effects going in opposite directions: (i) the bad convergence of the adiabatic PN expansion and (ii) the fact that the T4 approximant does not take into account non-adiabatic effects. This compensation causes an "enhancement" in the domain of validity of T4. However, we show that this enhancement holds only for a limited range of values of the mass ratio. This is consistent with the finding of [65] that the enhanced validity of T4 is fragile and is undone by spin effects.

In conclusion we think that the results presented here corroborate the aptness of the EOB formalism to provide accurate representations of general relativistic waveforms. We suggest that the specific 3^{+2}PN-accurate resummed EOB waveform (with the current "best-bet" values of the flexibility parameters determined here) be used in constructing banks of waveform templates for currently operating gravitational wave detectors.

APPENDIX A: COMPUTING METRIC WAVEFORMS FROM CURVATURE WAVEFORMS

This first appendix is devoted to the discussion of an appropriate way of choosing the integration constants that enter the metric waveform $h(t)$ when deriving it by double time integration from a given (numerical) curvature waveform $\psi_4(t)$.

Our conventions are as follows: for reasons of continuity with the recent papers [18,22,66] we use the normalization factor $N_\ell = \sqrt{(\ell+2)(\ell+1)\ell(\ell-1)}$ in the metric waveform to get the so-called Zerilli-Moncrief normalized waveform that we shall denote $\Psi_{\ell m}^{(e/o)}$ (for even and odd-parity) as used in Ref. [67]. The metric waveform is expanded in spin-weighted spherical harmonics of spin-weight $s = -2$ as

$$h_+ - \mathrm{i}h_\times = \sum_{\ell=2}^{\infty} \sum_{m=-\ell}^{\ell} h^{\ell m}{}_{-2}Y^{\ell m}(\theta, \phi), \qquad (A1)$$

where the link between the multipolar metric waveform $h_{\ell m}$ (as used for instance in [68]) is

$$h^{\ell m} = \frac{N_\ell}{r}(\Psi_{\ell m}^{(e)} + \mathrm{i}\Psi_{\ell m}^{(o)}). \qquad (A2)$$

The raw output of the numerical simulation used here is the Newman-Penrose scalar ψ_4. This is decomposed in harmonics as

$$\ddot{h}_+ - \mathrm{i}\ddot{h}_\times = \psi_4 = \sum_{\ell=2}^{\infty} \sum_{m=-\ell}^{\ell} \psi_4^{\ell m}{}_{-2}Y^{\ell m}(\theta, \phi). \qquad (A3)$$

The computation of the Zerilli metric multipoles from its curvature correspondant $\psi_4^{\ell m}$ requires a double time integration. Various ways of fixing the two integration constants entering this process have been discussed in the literature [15,62,69,70]. We focus here on the $\ell = m = 2$ multipole of the Zerilli-Moncrief normalized metric waveform $\Psi_{22}^{(e)}$.

We wish to emphasize that the choice of integration constants is particularly delicate when dealing with the metric waveform $h(t)$, by contrast to dealing with the quantity $\dot{h}(t)$ which is most prominent in other applications, such as the computation of recoil. For instance, Ref. [70] suggested to integrate backward in time starting with zero integration constants at $t = +\infty$. This procedure leads to a rather accurate $\dot{h}(t)$. However, we found that the resulting $h(t)$ is not accurate enough for the purpose of high-accuracy waveform comparison discussed in this paper. This is exemplified in Fig. 10. This figure shows the metric waveform obtained by such a backward integration. The important point is that the modulus of the complex
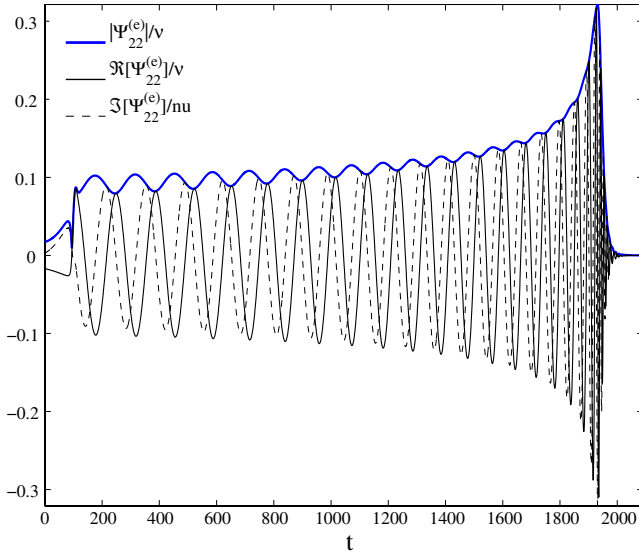
FIG. 10 (color online).   Computation of the Zerilli-normalized metric waveform $\Psi_{22}^{(e)}$ from $r\psi_4^{22}$ via two backward time integrations starting with zero integration constants at the final time. The data refer to the 1:1 mass ratio ($\nu = 0.25$) numerical simulation. Unphysical oscillations in the modulus are quite visible at early times.
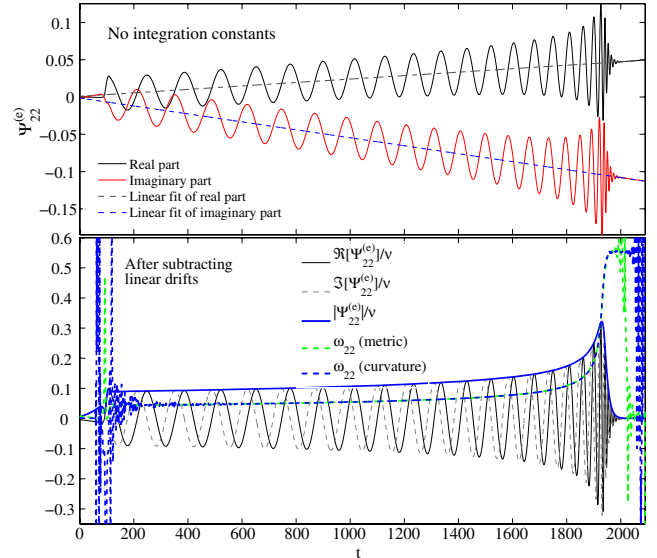

FIG. 11 (color online).   Computation of the metric waveform $\Psi_{22}^{(e)}$ from $r\psi_4^{22}$ via two time integrations starting at $t = 0$. The upper panel has zero integration constants and exhibits clear linear drifts $\alpha t + \beta$. The bottom panel shows the result of subtracting the linear drift of the waveform obtained by fitting the upper panel over the entire time interval starting at $t = 0$.

waveform exhibits quite visible unphysical oscillations at early times (during inspiral).

By contrast, we found that the following procedure (related to some of the suggestions of Ref. [62]) gave reliably accurate results. We start by computing (e.g., separately for the real and imaginary parts, or directly for the complex quantity) the first and second forward time integrals (using e.g. Simpson's rule) of $r\psi_4^{\ell m}$, starting at $t = 0$ with zero integration constants, i.e., we define

$$\dot{h}_0(t) = \int_0^t dt' r\psi_4^{\ell m}(t'), \qquad (A4)$$

$$h_0(t) = \int_0^t dt' \dot{h}_0(t'). \qquad (A5)$$

Then, we fit over the full simulation time interval (separately for the real and imaginary parts) the second integral $h_0(t)$ to a linear function of t, say $h_0^{\text{lin-fit}}(t) = \alpha t + \beta$ where α and β are complex quantities. Finally, we define the metric waveform as

$$h(t) \equiv h_0(t) - h_0^{\text{lin-fit}}(t) = h_0(t) - (\alpha t + \beta). \qquad (A6)$$

Note that this also defines the time derivative of the metric waveform as

$$\dot{h}(t) \equiv \dot{h}_0(t) - \alpha. \qquad (A7)$$

The result of this procedure is shown in Fig. 11. Here we applied the procedure explained above to the $r\psi_4^{22}$ waveform coming from the 1:1 mass-ratio simulation extracted at $r = 90$. The top panel shows the real and imaginary

parts of $h_0(t)$ (divided by the normalization factor N_2) together with their best linear fits, i.e. the real and imaginary parts of $\alpha t + \beta$. The bottom panel shows the final waveform $h(t)$, i.e. the difference between $h_0(t)$ and the best linear fit $\alpha t + \beta$. The important point is to notice that the modulus of $h(t)$ (the blue solid line in the bottom panel) is monotonically increasing with t during inspiral without exhibiting any of the unphysical oscillations that were present in the previous figure.[20] We show on the same plot also the real and imaginary parts of the complex quantity $\Psi_{22}^{(e)}$ (which correspond to the h_+ and $h_\times$ polarizations of the wave after division by r and multiplication by the spin-harmonic $_{-2}Y^{22}$) as well as the gravitational wave frequency ω_{22} obtained from the metric waveform $\Psi_{22}^{(e)}$ and the gravitational wave frequency obtained from the curvature waveform ψ_4^{22}.

In addition, let us emphasize that for this procedure to work it is important to start the integration from the absolute beginning of the numerical simulation, by which we really mean $t = 0$, i.e. before any signal reaches the observer. One might have thought that it is better to start the integration after the junk radiation, at the beginning of the inspiral signal. This is not the case, as it is illustrated in Fig. 12. This figure shows the worsened result we obtain when we use exactly the procedure explained above, but on

---

[20]This is a good indication that the integration constants have been computed correctly and that the real and the imaginary parts of the waveform are dephased by $\pi/2$ with very good approximation.
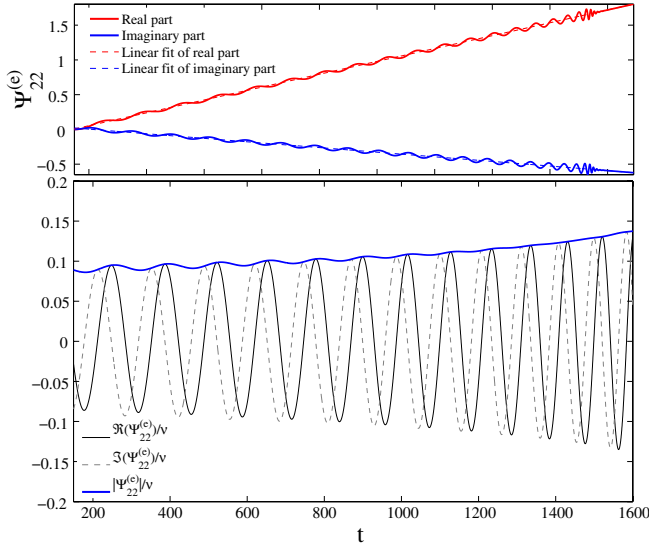
FIG. 12 (color online). Same as Fig. 11 except that the integration and the linear fit have been done starting at time $t \sim 150$, i.e. at the beginning of the inspiral signal. Note the oscillations in the modulus of the bottom panel, and the fact that the linear drifts (visible in the upper panel) are much larger than in Fig. 11.

the time interval $t \gtrsim 150$, i.e. starting at the beginning of the inspiral signal instead of starting at $t = 0$. Note the oscillations in the modulus of $\Psi_{22}^{(e)}$. By contrast, even if we blow up the corresponding graph in Fig. 11 the oscillations are practically absent. Note also that the linear drifts are now much larger than before. This is part of the reason why the results are less good in this case. By contrast to the first case where, starting at $t = 0$ meant starting with extremely small initial values of $r\psi_4^{22}$, starting at the beginning of the inspiral means starting with much larger values of $r\psi_4^{22}$: this effect enlarges the linear floors and therefore the errors on the determination of the linear floors to be subtracted.

APPENDIX B: SHORTCOMINGS OF THE TAYLORT4 PN APPROXIMANT

To contrast with the EOB-NR comparison done in the text, we consider in this appendix the comparison between the so-called TaylorT4 post-Newtonian approximant [23,25,28,65,71,72] and various NR data. This approximant is defined by two successive prescriptions: the first concerns the computation of a "T4 orbital phase" $\Phi_{T4}(t)$ while the second concerns the definition of a "T4 metric waveform." Here we shall focus only on the $\ell = m = 2$ quadrupolar waveform. The "T4 orbital phase" $\Phi_{T4}(t)$ is defined by integrating the ordinary differential equations

$$\frac{d\Phi_{T4}}{dt} = x^{3/2}, \qquad (B1)$$

$$\frac{dx}{dt} = \frac{64\nu}{5} x^5 a_{3.5}^{\text{Taylor}}, \qquad (B2)$$

where $a_{3.5}^{\text{Taylor}}$ is the 3.5 PN Taylor approximant, for any given value of ν, to the Newton-normalized ratio (flux-function)/(derivative of energy function) $=$ $\hat{F}(x)/\widehat{E'(x)}$ where $E'(x) = dE/dx$. As in the text, we scale dimensionful quantities by the total "bare" mass $M = m_1 + m_2$. This is for instance the case for the time variable t in the above equations. The explicit expression of $a_{3.5}^{\text{Taylor}}(x)$ reads [23,25] (for the nonspinning case)

$$a_{3.5}^{\text{Taylor}}(x) = 1 - \left(\frac{743}{336} + \frac{11}{4}\nu\right)x + 4\pi x^{3/2} \qquad (B3)$$

$$+ \left(\frac{34\,103}{18\,144} + \frac{13\,661}{2016}\nu\right)x^2 - \left(\frac{4159}{672} + \frac{189}{8}\nu\right)\pi x^{5/2}$$
$$+ \left[\frac{16\,447\,322\,263}{139\,708\,800} - \frac{1712}{105}\gamma - \frac{56\,198\,689}{217\,728}\nu + \frac{541}{896}\nu^2\right.$$
$$\left. - \frac{5605}{2592}\nu^3 + \frac{\pi^2}{48}(256 + 452\nu) - \frac{856}{105}\log(16x)\right]x^3$$
$$+ \left(-\frac{4415}{4032} + \frac{358\,675}{6048}\nu + \frac{91\,495}{1512}\nu^2\right)\pi x^{7/2}. \qquad (B4)$$

This phasing evolution is completed by a quadrupolar waveform which is known (for any given value of ν) at the 3 PN accuracy level [21,62,68,73]. Following [28,68] we define the 3 PN-accurate T4 waveform by dropping all the $\ln(x/x_0)$ terms in Eq. (79) of Ref. [68]. We display it explicitly here to clarify which waveforms we use in our T4 studies. The explicit expression of the $\ell = m = 2$ Zerilli-normalized metric waveform reads

$$\Psi_{22}^{T4} = -4\nu\sqrt{\frac{\pi}{30}}e^{-2i\Phi}x\left\{1 - x\left(\frac{107}{42} - \frac{55}{42}\nu\right) + 2\pi x^{3/2}\right.$$
$$- x^2\left(\frac{2173}{1512} + \frac{1069}{216}\nu - \frac{2047}{1512}\nu^2\right)$$
$$- x^{5/2}\left[\left(\frac{107}{21} - \frac{34}{21}\nu\right)\pi + 24i\nu\right]$$
$$+ x^3\left[\frac{27\,027\,409}{646\,800} + \frac{2}{3}\pi^2 + \frac{428}{105}[i\pi - 2\gamma_E\right.$$
$$- \ln(16x)] - \left(\frac{278\,185}{33\,264} - \frac{41}{96}\pi^2\right)\nu$$
$$\left.\left.- \frac{20\,261}{2772}\nu^2 + \frac{114\,635}{99\,792}\nu^3\right]\right\}. \qquad (B5)$$

where $\gamma_E = 0.577\,21\ldots$ is Euler's constant. The TaylorT4 3.5/2.5 waveform (used in most of our comparisons) is obtained by dropping the terms $\propto x^3[a\ln(x) + b]$ on the right-hand side of this equation.

Thorough comparisons between the TaylorT4 3.5/2.5 waveform (i.e., 3.5 PN accuracy for phase and 2.5 PN accuracy *only* for amplitude) and NR waveforms were performed, for the equal-mass case, $\nu = 0.25$, in [28,65,71]. Reference [28] concluded that this approximant yields an "astonishingly good" agreement with nu-

merical data during the inspiral, i.e. a dephasing smaller than 0.05 radians over ~30 GW cycles before reaching the GW frequency $M\omega_{22} = 0.1$. On the other hand, Ref. [65] showed that the inclusion of spins on the black holes had the effect of considerably worsening the agreement between T4 and NR data. Here we shall study the effect of varying the mass ratio (for nonspinnig black holes). We shall also go beyond the analyses of [28,71] in discussing the behavior of T4 for GW frequencies above 0.1. Let us first compare the[21] $\nu = 0.25$ TaylorT4 3.5/2.5 quadrupolar waveform Ψ_{22}^{T4} with equal-mass NR waveforms computed by the Jena group. As discussed in Sec. II, the BAM code outputs the Newman-Penrose curvature scalar $\psi_4(t, r, \theta, \varphi)$ at various extraction radii r. This angular-dependent curvature scalar is then: (i) decomposed on the basis of spin-weighted spherical harmonics and then (ii) integrated twice over time to yield the metric waveform Ψ_{22}^{NR}. The choice of integration constants in this integration procedure was done according to the procedure outlined in Appendix A. To compare the two waveforms Ψ_{22}^{NR} and Ψ_{22}^{T4}, as functions of their respective time variables, we choose a relative time shift τ and a relative phase shift α by following the same two-pinching-time procedure used in the text.

Figure 13 compares the gravitational wave frequency ω_{22} computed from the numerical data and plotted as a function of the NR time scale (solid line) with that of the TaylorT4 3.5/2.5 approximant plotted as a function of the shifted T4 time scale (dash-dot line). The two waveforms have been pinched at the NR times $t_1 = 1299.9$ and $t_2 = 1399.8$, corresponding to NR frequencies $\omega_1 = 0.062643$ and $\omega_2 = 0.066\,292$, respectively, (which approximate the matching frequency $\omega_m = \omega_3 = 0.063$ of [28]).

We see on this figure that there is a very good agreement between the two frequencies during the inspiral, up to, say, the NR time $t_{NR} = 1850$, where $\omega_{22}^{NR} = 0.1301$ and ω_{22}^{T4} differ by about 2.2%. Then, soon after, ω_{22}^{T4} starts deviating very strongly from ω_{22}^{NR} and *blows up to infinity* at the finite time $t_{blowup} = 1899.5$ (indicated by the leftmost vertical dashed line in the figure). This blowup time, considered on the NR time scale, corresponds to a NR frequency $\omega_{blowup}^{NR} \simeq 0.1889$. Note that this frequency is *smaller* than the effective-one-body GW frequency at the adiabatic LSO, which is equal to $2\Omega_{LSO}^{EOB} = 0.2114$ (corresponding to an EOB radial coordinate $r_{LSO}^{EOB} = 4.4729$). The rightmost vertical dashed line in the figure indicates the "ω-LSO", in the sense of Ref. [2], i.e. the time when the (NR) GW frequency ω_{22}^{NR} equals the adiabatic LSO frequency. Here we consider the case $\nu = 0.25$ and $a_5 = 25$ and we compute the LSO frequency within the EOB approach. Therefore, in the equal-mass case, the TaylorT4

---

[21]Here, to facilitate the comparison with previous work, we use a T4 approximant with 2.5 PN-accurate amplitude. Our main conclusions would be similar had we used the 3 PN-accurate amplitude.
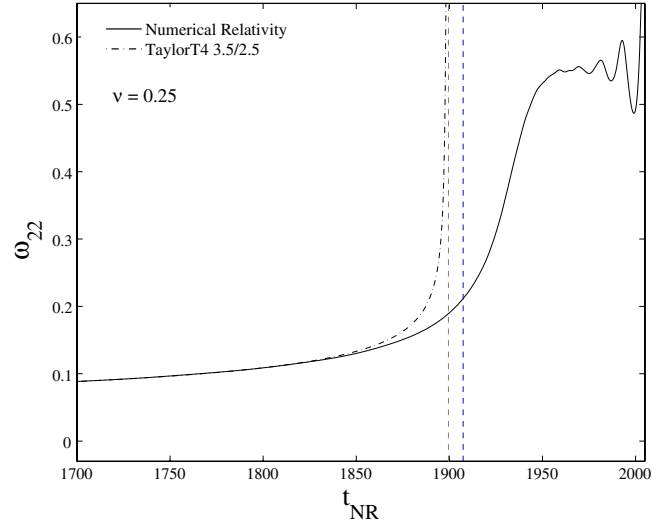

FIG. 13 (color online). Numerical relativity (Jena) and TaylorT4: comparison between the instantaneous gravitational wave frequencies for the equal-mass case ($\nu = 0.25$).

approximant breaks down already during late-inspiral, before the EOB LSO, and before the plunge.

The fact that the T4 approximant blows up at a finite time is a simple mathematical consequence of the structure of the differential equation (B2), given that, $a_{3.5}^{Taylor}(x)$ is found to remain positive for every $x \geq 0$. Indeed, one can even easily analytically compute the blowup time as being $t_{blowup} = t_0 + \Delta t$ where t_0 is any given "reference" time on the $T4$ time scale (corresponding to a frequency parameter $x(t_0) = x_0$), and where Δt is given by the following *convergent* integral

$$\Delta t = \int_{x_0}^{\infty} \frac{dx}{C_\nu x^5 a_{3.5}^{Taylor}}, \quad (B6)$$

where $C_\nu = 64\nu/5$.

After having compared the T4 approximant to NR data (in the equal-mass case) let us compare the T4 approximant to the EOB one. As emphasized in Ref. [21], a convenient way of comparing two waveforms (which avoids the issue of finding suitable time shifts and phase shifts) consists in considering the following shift-invariant "phase-acceleration" function

$$a_\omega(\omega) = \frac{\dot{\omega}}{c_\nu \omega^{11/3}}, \quad c_\nu = \frac{12}{5} 2^{1/3} \nu. \quad (B7)$$

Note that in the present paper we consider the frequencies of the *metric* waveforms (by contrast to the frequencies of the *curvature* waveforms considered in [21]).

In the left-panel of Fig. 14 we compare the phase-acceleration curves of T4 3.5/2.5 (dash-dot line) and EOB (solid line) for the equal-mass case. The leftmost vertical line indicates the EOB frequency ≈ 0.19 corresponding to the T4 blow-up time (computed by Eq. (B6)).
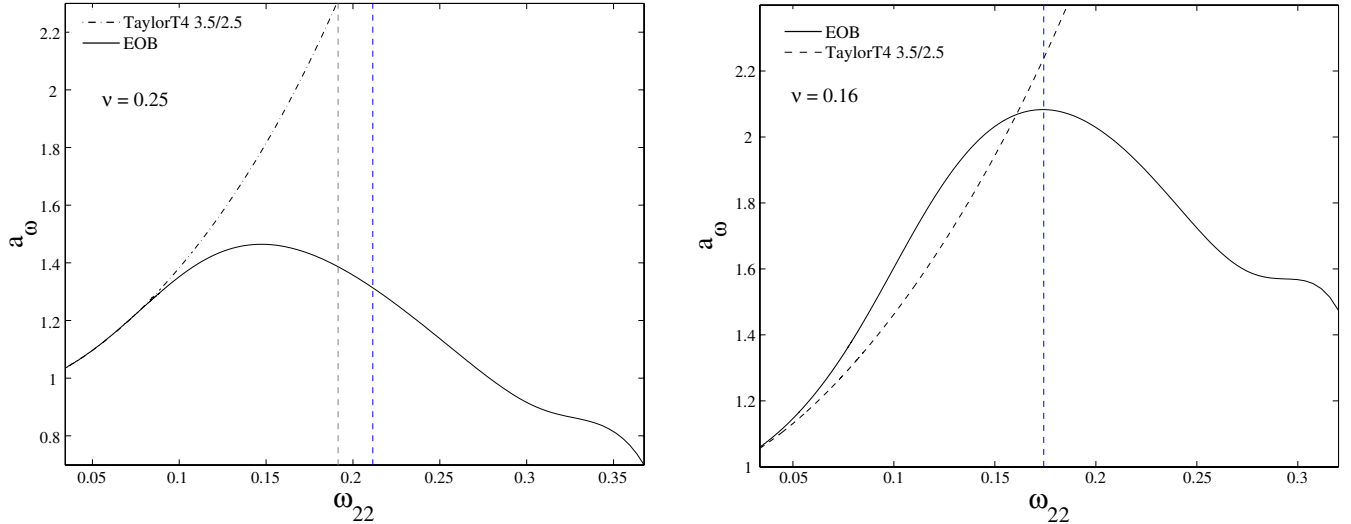
FIG. 14 (color online). Comparison between phase-acceleration curves a_ω of EOB (solid line) and TaylorT4 (dash-dot line) for $\nu = 0.25$ (left panel) and $\nu = 0.16$ (right panel). The rightmost dashed vertical line indicates the location of the EOB adiabatic LSO. The leftmost vertical line on the left panel indicates the EOB GW frequency corresponding the instant when T4 blows up.

The rightmost vertical line indicates the adiabatic EOB LSO frequency, $2\Omega_{\mathrm{LSO}}^{\mathrm{EOB}} \approx 0.21$ as above. We terminated the horizontal axis at $\omega_{22} = \omega_{22}^{\mathrm{LR}} = 0.3676$ which corresponds to the EOB time when the EOB orbital frequency reaches its maximum; i.e., the so-called "EOB light-ring," which defines the "merger time" within the EOB approach. Note that this figure shows the metric waveform analogue of the EOB (curvature) phase-acceleration curve of Fig. 2 of Ref. [21] and extends it up to the merger time. As was already emphasized in [21], the figure shows that the T4 acceleration curve strongly diverges away from the EOB one for frequencies $\omega_{22} \gtrsim 0.1$, i.e. during the late-inspiral, before reaching the LSO.

The right panel of Fig. 14 illustrates the case where the mass ratio is 4:1, i.e. $\nu = 0.16$. The vertical dashed line indicates the adiabatic EOB LSO frequency $2\Omega_{\mathrm{LSO}}^{\mathrm{EOB}} \approx 0.17$. For this value of ν, the blowup frequency, computed as above, turns out to be larger than the EOB light-ring frequency $\omega_{22}^{\mathrm{LR}} = 0.3201$. We see on this plot that, contrary to the equal-mass case, the T4 acceleration curve starts to deviate significantly from the EOB one for frequencies $\omega_{22} \gtrsim 0.05$. Note, however, that because the two curves cross again just before the LSO, we expect that the phase difference between T4 and EOB will remain, on average, rather small up to the LSO. However later on the T4 phasing will drastically deviate from the EOB one.

Finally, Fig. 15 considers the test-mass limit ($\nu \to 0$). Here we compare three acceleration curves: (i) the *adiabatic* limit of the T4 acceleration curve, given simply by $a_\omega(\omega) = a_{3.5}^{\mathrm{Taylor}}(x)$ computed in the limit $\nu \to 0$ and with $x = (\omega/2)^{2/3}$; (ii) the EOB a_ω curve computed for $\nu = 0.01$, and (iii) the exact adiabatic limit of the test-mass acceleration curve, i.e. the Newton-normalized ratio

$\hat{F}(x)/\widehat{E'(x)}$ (see e.g. Ref. [7]). Here the flux function $\hat{F}(x)$ is the one computed numerically in Refs. [74,75]. The two vertical lines in the figure refer to the $\nu = 0$ limit of the adiabatic LSO frequency (leftmost line, $2\Omega = 0.1361$) and to the $\nu = 0.01$ EOB adiabatic LSO frequency (rightmost line, $2\Omega_{\mathrm{LSO}} = 0.1378$). This figure illustrates two facts: first, the T4 approximant starts strongly deviating from the exact result early on (say for $\omega_{22} \lesssim 0.06$, see inset); second, one needs to consider $\nu < 0.01$ to ensure that the usual adiabatic approximation is satisfactory up to frequen-
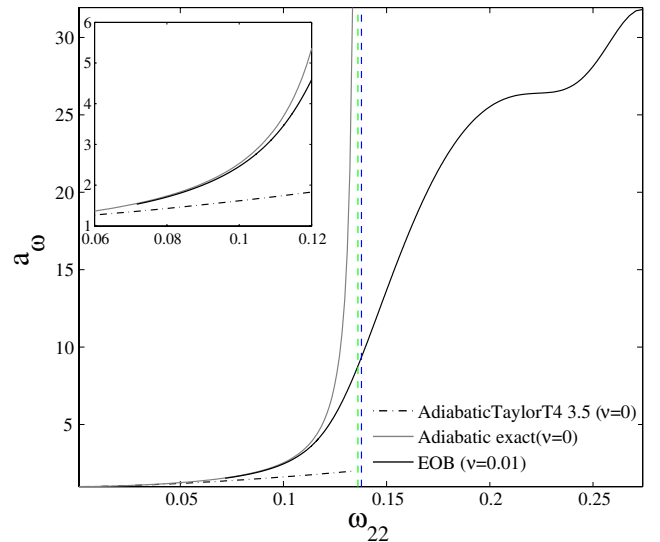

FIG. 15 (color online). This figure (done for $\nu \ll 1$) illustrates, in particular, the fact that the domain of validity of TaylorT4 when $\nu \lesssim 0.16$ reduces to the "normal" 3.5 PN one, namely $\omega \lesssim 0.06$.

cies close to the LSO one. This is consistent with the analytical estimate obtained in [2] according to which the deviations from adiabaticity become important when the frequency fractionally deviates from the LSO frequency by $\delta\omega/\omega_{\mathrm{LSO}} \sim \nu^{2/5}$. The presence of the 2/5 power means that we need $\nu \lesssim 3 \times 10^{-3}$ to be approximately adiabatic up to 90% of the LSO frequency.

Summarizing, the main results of the present appendix (and of complementary investigations of the different ''speeds'' with which the T4 and EOB waveforms ''move'' as ν varies) are: (i) we predict that the T4 approximant will define an *effective* phasing template for the *inspiral* waveform only up to some ν-dependent upper GW frequency, say $\omega_{\max}^{\mathrm{T4}}(\nu)$, having the following properties; (ii) for $\nu = 0.25$, $\omega_{\max}^{\mathrm{T4}}(0.25) \approx 0.14$ (consistently with [28]) which is significantly above the expected range of validity of a normal PN approximant, but still significantly below the (EOB-estimated[22]) gravitational wave LSO frequency $\omega_{\mathrm{LSO}}^{\mathrm{EOB}} = 0.2114$. For $\nu = 0.16$, the upper bound *increases* to $\omega_{\max}^{\mathrm{T4}}(0.16) \approx 0.17$, i.e. around the corresponding LSO frequency. For intermediate values $0.16 \lesssim \nu \lesssim 0.25$, the situation smoothly interpolates between these two cases; (iii) by contrast, as ν gets smaller than about 0.16, $\omega_{\max}^{\mathrm{T4}}(\nu)$ will decrease down to values of order of 0.05, which are typical of the expected upper

_____

[22]For the reasons discussed above, our EOB estimates here use $a_5 = 25$.

frequency of validity for a normal PN approximant[23]; (iv) in all cases the range of validity of T4 is limited to the inspiral and, contrary to the EOB, does not include the plunge; (v) in all cases, T4 exhibits a blowup of the frequency at a finite time. However, this blowup is not always the main reason limiting the validity of the approximant. For instance, this is the case when $\nu \approx 0.25$, but not when $\nu \lesssim 0.16$. Let us finally emphasize that the enhancement in the domain of validity of T4 when $0.16 \lesssim \nu \lesssim 0.25$ with respect to the normal expected PN validity is due to a *lucky compensation* (which does not take place when $\nu \lesssim 0.16$) between two effects going in opposite directions: on the one hand, the bad convergence of the adiabatic PN expansion; on the other hand, the fact that the T4 approximant does not take into account nonadiabatic effects (which are quite significant as emphasized in [2] and displayed in Fig. 2 of [21]). Our present result clarifies the theoretical underpinnings of the result found in [65], namely, that ''deformation'' of the T4 approximant by spin effects removes the accidental nice agreement between T4 and NR. Indeed, one should not expect such a chance compensation to be stable under any deformation of the underlying physics (such as additional spins or a varying mass ratio).

_____

[23]Indeed, Ref. [76] estimated the (3 PN-accurate) ''PN failure point'' to be around $\Omega^{1/3} \approx 0.3$ which corresponds to $\omega_{22} = 2\Omega = 0.054$.

[1] A. Buonanno and T. Damour, Phys. Rev. D **59**, 084006 (1999).
[2] A. Buonanno and T. Damour, Phys. Rev. D **62**, 064015 (2000).
[3] T. Damour, P. Jaranowski, and G. Schaefer, Phys. Rev. D **62**, 084011 (2000).
[4] T. Damour, Phys. Rev. D **64**, 124013 (2001).
[5] L. Blanchet, Living Rev. Relativity **9**, 4 (2006), http://www.livingreviews.org/lrr-2006-4.
[6] E. Brezin, C. Itzykson, and J. Zinn-Justin, Phys. Rev. D **1**, 2349 (1970).
[7] T. Damour, B. R. Iyer, and B. S. Sathyaprakash, Phys. Rev. D **57**, 885 (1998).
[8] M. Davis, R. Ruffini, and J. Tiomno, Phys. Rev. D **5**, 2932 (1972).
[9] A. Buonanno, Y. Chen, and T. Damour, Phys. Rev. D **74**, 104005 (2006).
[10] F. Pretorius, arXiv:0710.1338.
[11] F. Pretorius, Phys. Rev. Lett. **95**, 121101 (2005).
[12] M. Campanelli, C. O. Lousto, P. Marronetti, and Y. Zlochower, Phys. Rev. Lett. **96**, 111101 (2006).
[13] J. G. Baker, J. Centrella, D.-I. Choi, M. Koppitz, and J. van Meter, Phys. Rev. Lett. **96**, 111102 (2006).
[14] J. A. Gonzalez, U. Sperhake, B. Bruegmann, M. Hannam,

and S. Husa, Phys. Rev. Lett. **98**, 091101 (2007).
[15] M. Koppitz, D. Pollney, and R. Christian, Phys. Rev. Lett. **99**, 041102 (2007).
[16] T. Damour, E. Gourgoulhon, and P. Grandclement, Phys. Rev. D **66**, 024007 (2002).
[17] T. Damour, B. R. Iyer, P. Jaranowski, and B. S. Sathyaprakash, Phys. Rev. D **67**, 064028 (2003).
[18] T. Damour and A. Nagar, Phys. Rev. D **76**, 064028 (2007).
[19] T. Damour, P. Jaranowski, and G. Schafer, Phys. Lett. B **513**, 147 (2001).
[20] A. Buonanno *et al.*, Phys. Rev. D **76**, 104049 (2007).
[21] T. Damour and A. Nagar, Phys. Rev. D **77**, 024043 (2008).
[22] T. Damour, A. Nagar, E. N. Dorband, D. Pollney, and L. Rezzolla, Phys. Rev. D **77**, 084017 (2008).
[23] A. Buonanno, G. B. Cook, and F. Pretorius, Phys. Rev. D **75**, 124018 (2007).
[24] T. Damour and A. Nagar, Phys. Rev. D **76**, 044003 (2007).
[25] Y. Pan *et al.*, Phys. Rev. D **77**, 024014 (2008).
[26] T. Damour and A. Gopakumar, Phys. Rev. D **73**, 124006 (2006).
[27] T. Damour, P. Jaranowski, and G. Schafer, Phys. Rev. D **78**, 024009 (2008).
[28] M. Boyle *et al.*, Phys. Rev. D **76**, 124038 (2007).
[29] T. Damour, B. R. Iyer, and B. S. Sathyaprakash, Phys. Rev.

D **63**, 044023 (2001).

[30] B. Brügmann, J. A. González, M. Hannam, S. Husa, U. Sperhake, and W. Tichy, Phys. Rev. D **77**, 024027 (2008).

[31] S. Husa, J. A. Gonzalez, M. Hannam, B. Brugmann, and U. Sperhake, Classical Quantum Gravity **25**, 105006 (2008).

[32] M. Hannam, S. Husa, J. A. González, U. Sperhake, and B. Brügmann, Phys. Rev. D **77**, 044020 (2008).

[33] D. S. Brill and R. W. Lindquist, Phys. Rev. **131**, 471 (1963).

[34] R. Beig and N. O'Murchadha, Classical Quantum Gravity **11**, 419 (1994).

[35] R. Beig and S. Husa, Phys. Rev. D **50**, R7116 (1994).

[36] S. Brandt and B. Brügmann, Phys. Rev. Lett. **78**, 3606 (1997).

[37] S. Dain and H. Friedrich, Commun. Math. Phys. **222**, 569 (2001).

[38] M. Hannam, S. Husa, D. Pollney, B. Brugmann, and N. O'Murchadha, Phys. Rev. Lett. **99**, 241102 (2007).

[39] M. Hannam, S. Husa, N. Ó Murchadha, B. Brügmann, J. A. González, and U. Sperhake, J. Phys. Conf. Ser. **66**, 012047 (2007).

[40] M. Hannam, S. Husa, F. Ohme, B. Brugmann, and N. O'Murchadha, arXiv:0804.0628 [Phys. Rev. D (to be published)].

[41] J. M. Bowen and J. W. York, Phys. Rev. D **21**, 2047 (1980).

[42] S. Dain, Phys. Rev. Lett. **87**, 121102 (2001).

[43] M. Hannam, S. Husa, B. Brügmann, J. A. Gonzalez, and U. Sperhake, Classical Quantum Gravity **24**, S15 (2007).

[44] E. Schnetter, B. Krishnan, and F. Beyer, Phys. Rev. D **74**, 024028 (2006).

[45] K. A. Dennison, T. W. Baumgarte, and H. P. Pfeiffer, Phys. Rev. D **74**, 064016 (2006).

[46] W. Tichy and B. Brügmann, Phys. Rev. D **69**, 024006 (2004).

[47] D. Christodoulou, Phys. Rev. Lett. **25**, 1596 (1970).

[48] D. Christodoulou and R. Ruffini, Phys. Rev. D **4**, 3552 (1971).

[49] M. Ansorg, B. Brügmann, and W. Tichy, Phys. Rev. D **70**, 064011 (2004).

[50] S. Husa, M. Hannam, J. A. González, U. Sperha ke, and B. Brügmann, Phys. Rev. D **77**, 044037 (2008).

[51] L. Blanchet, G. Faye, B. R. Iyer, and B. Joguet, Phys. Rev. D **65**, 061501 (2002).

[52] L. Blanchet, T. Damour, G. Esposito-Farese, and B. R. Iyer, Phys. Rev. Lett. **93**, 091101 (2004).

[53] M. Shibata and T. Nakamura, Phys. Rev. D **52**, 5428 (1995).

[54] T. W. Baumgarte and S. L. Shapiro, Phys. Rev. D **59**, 024007 (1998).

[55] C. Bona, J. Massó, E. Seidel, and J. Stela, Phys. Rev. Lett. **75**, 600 (1995).

[56] M. Alcubierre, B. Brügmann, D. Pollney, E. Seidel, and R. Takahashi, Phys. Rev. D **64**, 061501(R) (2001).

[57] M. Alcubierre, B. Brügmann, P. Diener, M. Koppitz, D. Pollney, E. Seidel, and R. Takahashi, Phys. Rev. D **67**, 084023 (2003).

[58] E. T. Newman and R. Penrose, J. Math. Phys. (N.Y.) **3**, 566 (1962); **4**, 998(E) (1963).

[59] J. M. Stewart, *Advanced General Relativity* (Cambridge University Press, Cambridge, England, 1990).

[60] L. E. Kidder, Report presented at PN2008 Jena conference, http://www.sfb.tpi.uni-jena.de/Events/PN2008/PN2008_Program.shtm (2008).

[61] E. Berti, V. Cardoso, and C. M. Will, Phys. Rev. D **73**, 064030 (2006).

[62] E. Berti *et al.*, Phys. Rev. D **76**, 064034 (2007).

[63] T. Damour, Int. J. Mod. Phys. A **23**, 1130 (2008).

[64] W. Press and S. A. Teukolsky, Astrophys. J. **185**, 649 (1973).

[65] M. Hannam, S. Husa, B. Brügmann, and A. Gopakumar, arXiv:0712.3787.

[66] A. Nagar, T. Damour, and A. Tartaglia, Classical Quantum Gravity **24**, S109 (2007).

[67] A. Nagar and L. Rezzolla, Classical Quantum Gravity **22**, R167 (2005).

[68] L. E. Kidder, Phys. Rev. D **77**, 044016 (2008).

[69] D. Pollney *et al.*, Phys. Rev. D **76**, 124002 (2007).

[70] J. D. Schnittman *et al.*, Phys. Rev. D **77**, 044031 (2008).

[71] J. G. Baker, J. R. van Meter, S. T. McWilliams, J. Centrella, and B. J. Kelly, Phys. Rev. Lett. **99**, 181101 (2007).

[72] A. Gopakumar, M. Hannam, S. Husa, and B. Brügmann, arXiv:0712.3737.

[73] K. G. Arun, L. Blanchet, B. R. Iyer, and M. S. S. Qusailah, Classical Quantum Gravity **21**, 3771 (2004).

[74] C. Cutler, E. Poisson, G. J. Sussman, and L. S. Finn, Phys. Rev. D **47**, 1511 (1993).

[75] E. Poisson, Phys. Rev. D **52**, 5719 (1995).

[76] P. R. Brady, J. D. E. Creighton, and K. S. Thorne, Phys. Rev. D **58**, 061501 (1998).